The Astrophysical Journal, 945:97 (23pp), 2023 March 10 https://doi.org/10.3847/1538-4357/acb5e9
© 2023. The Author(s). Published by the American Astronomical Society.
OPEN ACCESS

The Differential Assembly History of the Centers and Outskirts of Main-sequence Galaxies at $z \sim 2.3$

Sam E. Cutler, Mauro Giavalisco, Zhiyuan Ji, and Yingjie Cheng
Department of Astronomy, University of Massachusetts, Amherst, MA 01003, USA; secutler@umass.edu
Received 2022 August 1; revised 2023 January 5; accepted 2023 January 23; published 2023 March 10

Abstract

We present a study of spatially resolved star formation histories (SFHs) for 60 $z \sim 2.3$ main-sequence, star-forming galaxies selected from the MOSDEF spectroscopic survey in the GOODS-N field, with median stellar mass $\log(M_\star/M_\odot) = 9.75$ and spanning the range $8.6 < \log(M_\star/M_\odot) < 11.5$. Photometry is decomposed into a central and an outer spatial component using observed $z_{\rm F850LP} - H_{\rm F160W}$ colors. The PROSPECTOR code is used to model spectral energy distributions for the center, outskirt, and integrated galaxy using Hubble Space Telescope/ACS and WFC3, Spitzer/IRAC, and ground-based photometry, with additional constraints on gas-phase metallicity and spectroscopic redshift from MOSDEF spectroscopy. For the low-resolution bands, spatially resolved photometry is determined with an iterative approach. The reconstructed SFHs indicate that the majority of galaxies with $\log(M_\star/M_\odot) < 10.5$ are observed while their central regions undergo relatively recent (<100 Myr) bursts of star formation, whereas the outskirts have a smooth, quasi-steady SFH that gently increases toward the redshift of observation. The enhanced star formation activity of the central parts is broadly consistent with the idea that it is produced by highly dissipative gas compaction and accretion. The wide range of central densities and sizes observed in the sample suggests that, for the selected galaxies, such a process has started but is still far from being completed. The implication would be that selecting star-forming galaxies at cosmic noon frequently includes systems in an "evolved" evolutionary phase where the centers have recently started a burst of star formation activity that will likely initiate inside-out quenching in the next several hundred million years.

Unified Astronomy Thesaurus concepts: Galaxy evolution (594); Galaxy formation (595); Spectral energy distribution (2129)

1. Introduction

A fundamental question in galaxy evolution is the formation history of the dense stellar cores associated with galactic bulges. In the canonical picture, galaxy growth and quenching is an inside-out process. Massive galaxies ($>10^{11}\,M_\odot$) build their outer regions (i.e., increase in size) at lower redshift (van Dokkum et al. 2010; Whitney et al. 2019; Mosleh et al. 2020; Cutler et al. 2022; Ji & Giavalisco 2022) whereas the central parts of these galaxies are in place as early as $z \sim 2$ (Carrasco et al. 2010). Similar studies have shown this inside-out growth is prominent in galaxies across the main sequence and even below the main sequence (e.g., van der Wel et al. 2014a; Nelson et al. 2016; Dimauro et al. 2022). The prominence of galactic bulges is correlated both with the stellar mass of the galaxy and scale length of the disk (Shen et al. 2003; van der Wel et al. 2014a), indicating that the growth of the disk is tied to the formation and structure of the bulge. Similarly, the growth of the central supermassive black hole in galaxies is also correlated with the bulge strength (Häring & Rix 2004; Kormendy & Ho 2013), which suggests that the bulge may play a role in active galactic nuclei (AGNs) strength and corresponding quenching processes (Chen et al. 2020). Bulges have also been tied to slow, inside-out quenching processes, in which massive bulges stabilize the gas in the disk and prevent it from collapsing in a process called "morphological quenching" (Martig et al. 2009). Further studies suggest that the bending of the star-forming main sequence (SFMS) to lower specific star formation rates ($\rm sSFR \equiv SFR/M_\star$) at higher stellar mass is evidence of the presence of old bulges in massive galaxies (Abramson et al. 2014), though this is disputed (e.g., Guo et al. 2015; Schreiber et al. 2016; Dimauro et al. 2022).

Dense stellar cores have been directly observed in the optical and near-infrared (NIR) for the most massive galaxies as early as $z \sim 2.5$ (e.g., Carrasco et al. 2010; van Dokkum et al. 2014). Analysis of the mass evolution in these optically detected galaxies suggests it predominantly occurs in the outer stellar envelope, while these central regions maintain a roughly constant mass (e.g., van Dokkum et al. 2014). The forming dense stellar cores of massive, main-sequence galaxies have also been probed using observations of obscured star formation with the Atacama Large Millimeter/submillimeter Array. These studies found dense, starbursting cores that likely formed at the centers of extended disks, due to dissipative collapse (e.g., Tadaki et al. 2017, 2020), suggesting an outside-in formation process counter to that suggested by van Dokkum et al. (2014). Alternatively, mergers could play a significant role in forming compact starburst regions by driving gas into the galactic center (Puglisi et al. 2019, 2021). These centrally concentrated starbursts may reflect the final stage of star formation before quiescence (Elbaz et al. 2018) and have very short depletion times, which become even shorter for more compact systems (Franco et al. 2020; Gómez-Guijarro et al. 2022).

On the other hand, the low dark matter fractions measured in these galaxies are similar to those of $z = 0$ massive, fast-rotating ellipticals, suggesting these star-forming galaxies may be the progenitors of today's massive ellipticals

Original content from this work may be used under the terms of the Creative Commons Attribution 4.0 licence. Any further distribution of this work must maintain attribution to the author(s) and the title of the work, journal citation and DOI.

(Genzel et al. 2017, 2020). Moreover, there is not clear observational evidence for the direct detection of distinct centers in less massive, potential Milky Way progenitors at higher redshifts. In contrast to the results of massive galaxy studies, some observations suggest that cores are not fully formed in Milky Way progenitors at high redshift and significant mass evolution occurs at all radii (van Dokkum et al. 2013). In this scenario, bulges likely form alongside disks through migration of star-forming clumps (Dekel et al. 2009a, 2009b). This is driven by the accretion of cold gas filaments into the disk (as seen in simulations; Kereš et al. 2005). The massive amount of gas entering the disk subsequently fragments into dense clumps through violent disk instabilities, and these clumps become sites of intense bursts of star formation. Dynamical friction then causes these clumps to migrate to the center of the galaxy and then merge to form a bulge (Dekel et al. 2009a, 2009b; Ceverino et al. 2015; Mandelker et al. 2017; Renzini 2020). Observations support this formation pathway, as clumps closer to galactic centers tend to be older and less active (Guo et al. 2012), though other secular evolution processes (e.g., bar instabilities; Kormendy & Kennicutt 2004) may also play a role.

In another scenario, a compaction event causes the dissipative collapse of cold gas into the galactic center (Dekel & Burkert 2014; Zolotov et al. 2015; Tacchella et al. 2018; Nelson et al. 2019b). The so-called wet disk contraction triggers a burst of star formation in the center of the galaxy, resulting in a so-called "blue nugget." Compaction events can be caused by a number of physical mechanisms, including violent disk instabilities triggered by cold gas accretion (Dekel & Burkert 2014), mergers (which can also cause disk instabilities; see Zolotov et al. 2015; Inoue & Inutsuka 2016), and collisions of counter-rotating streams (Dekel et al. 2019). The removal of gas from the disk, as well as other internal (star formation and AGN feedback) or external (halo heating of CGM gas) processes, then leads to the galaxy quenching. However, the galaxies may only stay quenched permanently if they have reached a certain cutoff in halo mass and the CGM is heated to the point where cold-mode accretion stops. If this threshold is not reached, these galaxies may be able to regrow their disks (Tacchella et al. 2016). This could explain the discrete bimodal distribution seen in chemical diagrams of the Milky Way center (Queiroz et al. 2020): α-rich, metal-poor populations (the bulge and chemical thick disk) are formed in an early burst caused by gas contraction, which briefly causes the galaxy to quench and eject gas out of the galactic center—then cold-mode accretion resumes, forming an α-poor, metal-enhanced population in the thin disk that mixes into the bulge/thick disk over time.

The progenitors of today's Milky Way/L^* galaxies are less massive than the galaxies studied in Genzel et al. (2017) or Genzel et al. (2020). Due to their location in the middle of the SFMS, lower-mass ($\log(M_\star/M_\odot) < 11$ UV/optically selected galaxies have been identified as potential candidates for progenitors of Milky Way–like galaxies (Giavalisco et al. 1996; Steidel et al. 1996; Papovich et al. 2001; Shapley et al. 2001; Giavalisco 2002; Steidel et al. 2010; Williams et al. 2014). Moreover, chemical and kinematic studies of the bulge of the Milky Way in Queiroz et al. (2021) suggest that the bulge is most likely an old, pressure-supported component, which formed around $z \sim 2$–3. As such, observations of these lower-mass, UV/optically selected galaxies galaxies between $2 < z < 3$ could reveal forming bulges and dense centers and help constrain the physical processes behind bulge formation in lower-mass galaxies. In this paper, we search for these objects in a sample of UV-bright, low-obscuration, star-forming galaxies at $z \sim 2.3$ in the Great Observatories Origins Deep Survey-North (GOODS-N).

It is important to note that, throughout this paper, the terms "centers" or "cores" are used in lieu of "bulges" to refer to the compact and dense central regions of the galaxies under consideration, as "bulge" may invoke the stricter definition of a classical bulge (or pseudobulge) used in connection to local galaxies. In the Milky Way, this central component includes the chemical thick disk, which is also believed to form around $2 < z < 3$ and is confined to the inner few kpc of the galaxy (Miglio et al. 2021; Queiroz et al. 2021). Thus, the centers in this paper refer to the central regions of the galaxies with no consideration, in defining the term, to their star formation activity, age, metallicity, light profile, or dynamical state, and likely includes significant contributions from a forming bulge and thick disk. In fact, the primary goal of this paper is to investigate if the central regions of star-forming galaxies at the cosmic noon that are plausible candidates for today's MW–like galaxies are already characterized by a different star formation history than the outer regions. Similarly, the term "outskirts" is used instead of "disk," as this refers to the outer regions of the galaxy, which likely covers the thin disk with some contamination from the outer thick disk.

We reconstruct the star formation history of our target galaxies using the fully Bayesian PROSPECTOR code (Johnson et al. 2021), which we use to fit the sensitive CANDELS (Grogin et al. 2011; Koekemoer et al. 2011) panchromatic spectral energy distributions (SEDs) of the two resolved, color-selected subcomponents, the center and the outskirts, to spectral populations synthesis evolution models. To achieve the most accurate age measurements possible, we also use spectroscopic redshift and gas-phase metallicity measures for our galaxies from the MOSFIRE Deep Evolution Field (MOSDEF) spectroscopic survey (Kriek et al. 2015) as strong priors in the fits. MOSDEF is also biased toward UV-selected galaxies (due to the lower spectroscopic success rate for red galaxies), which provides ideal targets for this study. Metallicity measurements, along with coverage in the observed infrared (IR) from Spitzer/IRAC can help break the age–metallicity degeneracy, while the rest-frame optical spectroscopy also provides accurate redshifts for SED fitting.

The primary goal of this study is to study the star formation history of the central regions and outskirts of our targets to help provide empirical constraints on the mechanisms of their assembly. If the central regions of these galaxies have been following substantially different evolutionary path than the outskirts, we should see this in the resulting star formation histories (SFHs): centers could form earlier than or coevally with the outskirts, but most models expect the formation to be bursty, occur later on, and decline faster than the outer region (Dekel et al. 2009a; Guo et al. 2012; Franco et al. 2020; Dimauro et al. 2022), potentially in an outside-in fashion, i.e., with centers exhibiting a declining and sharply peaked SFH when compared to the outer components.

In Section 2, we describe the photometric and spectroscopic data used in SED fitting and core decomposition. Section 3 explains the techniques used to decompose galaxies into resolved central and outer components and deal with

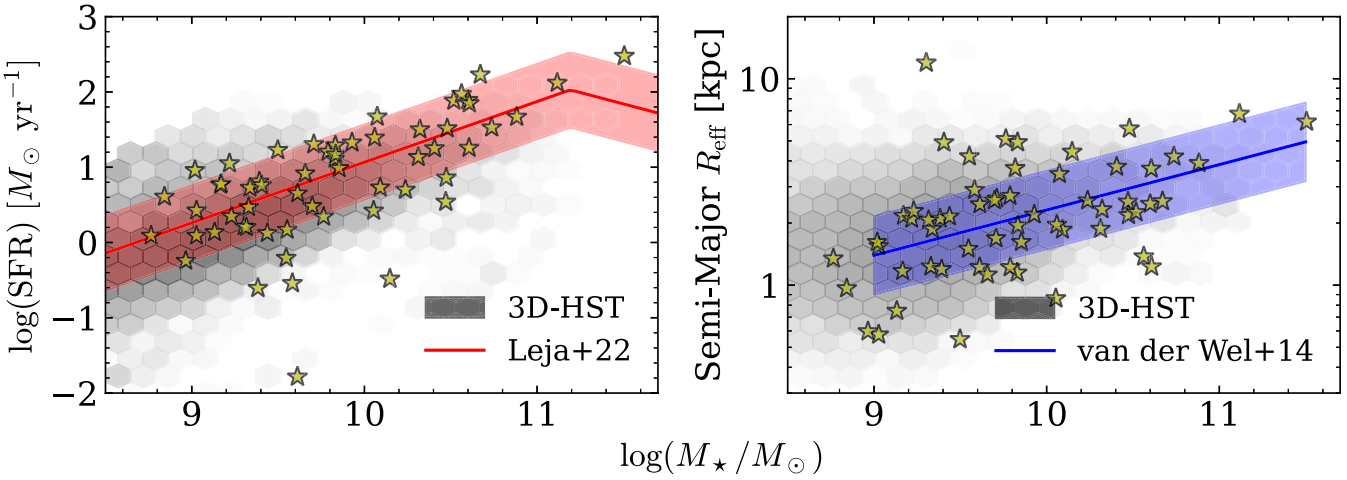

Figure 1. Location of sample galaxies (yellow stars) on the SFMS (left) and the star-forming galaxy size–mass relation (right). Galaxies in this sample occupy the middle of the SFMS at $z\sim2.3$ and fall within the scatter of the size–mass relation. Gray hexbins indicate an underlying sample of galaxies from the 3D-HST morphological catalog (van der Wel et al. 2014b). The SFMS from Leja et al. (2022) is shown with a 0.5 dex scatter in red, and the size–mass relation and intrinsic size scatter of 0.19 dex are from van der Wel et al. (2014b). This sample contains an overabundance of compact galaxies (>0.19 dex below the size–mass relation).

unresolved photometry (K-band/IRAC), as well as the PROSPECTOR model we use to fit SEDs. We discuss the resulting SFHs and their impact on our understanding of galaxy formation in Section 4. A summary of our conclusions is presented in Section 5. Throughout the paper, we assume a flat ΛCDM cosmology with $\Omega_m=0.3$, $\Omega_\Lambda=0.7$, and $H_0=70\,\mathrm{km\,s^{-1}\,Mpc^{-1}}$, as well as a Kroupa initial mass function (Kroupa 2001) for stellar masses. All magnitudes are in the AB system.

2. Data and Sample Selection

Our sample consists of 60 $z\sim2.3$ galaxies from the GOODS-N field. GOODS-N is chosen because it has both rest-frame optical spectroscopy from MOSDEF (Kriek et al. 2015) and photometric measurements ranging from the rest-frame ultraviolet (UV) to mid-IR (MIR). The sample of galaxies is chosen by matching sources without photometric contamination by other adjacent sources (FLAGS = 0) from the the multiwavelength Hubble Space Telescope (HST) $H_{\rm F160W}$-selected CANDELS/SHARDS catalogs of Barro et al. (2019) to a sample of MOSDEF galaxies from Sanders et al. (2018), which has robust spectroscopic redshifts and metallicities measured at $z\sim2.3$. Roughly 5% of the Barro et al. (2019) catalog is removed by applying the contamination flags selection. Of this uncontaminated sample, only 464 galaxies (1.3%) have MOSDEF coverage, and 63 of those are in the metallicity sample from Sanders et al. (2018). The Sanders et al. (2018) sample also removes potential AGN using mid-IR (MIR) Spitzer/IRAC selections presented in Coil et al. (2015), as well as X-ray and emission line selections. Figure 1 shows the final sample of galaxies relative to the SFMS (left) and the galaxy size–mass relation (right). These galaxies have an average stellar mass of $\log(M_\star/M_\odot)=9.75\pm0.29$ and an average size of $R_{\rm eff}=2.16\pm1.86$ kpc. The median SFR is $\dot{M}=39.2\pm26.5\,M_\odot\,\mathrm{yr^{-1}}$ on a 100 Myr timescale and $\dot{M}=7.5\pm6.1\,M_\odot\,\mathrm{yr^{-1}}$ on a 10 Myr timescale. Stellar masses and SFRs are measured from the global PROSPECTOR fits discussed in Section 3, and sizes are taken from the 3D-HST morphological catalogs (van der Wel et al. 2014b). In general, the galaxies span a wide range of masses and SFRs, covering most of the SFMS at $z\sim2.3$. These galaxies also generally fall within the intrinsic size scatter (0.19 dex) of the $z=2.25$ star-forming galaxy size–mass relation from van der Wel et al. (2014b), though 17% of the sample lies >0.19 dex below the relation, suggesting a slight overabundance of compact galaxies.

2.1. Photometric Data

Photometric data are taken directly from the CANDELS/SHARDS catalogs (Barro et al. 2019) for each cross-matched galaxy. In the UV, we include Kitt Peak North U-band photometry from the Hawaii Hubble Deep Field North survey (Capak et al. 2004). The optical photometry is composed of HST/ACS observations in the F435W, F606W, F775W, and F850LP filters from GOODS (Giavalisco et al. 2004), as well as F814W from CANDELS (Grogin et al. 2011; Koekemoer et al. 2011). CANDELS data are also used in the NIR with the HST/WFC3 F105W, F125W, and F160W filters, with additional NIR measurements coming from HST/WFC3 F140W in the AGHAST survey GO: 11600 (PI: B. Weiner) and Subaru/MOIRCS K-band (Kajisawa et al. 2011). The photometry is rounded out by MIR Spitzer/IRAC observations in the 3.6, 4.5, 5.6, and 8 μm filters (Dickinson et al. 2003; Ashby et al. 2013). Stellar masses from the catalog are also included as initial estimates for the stellar mass of the galaxy. These masses are derived with the FAST code (Kriek et al. 2009).

2.2. Spectroscopic and Metallicity Data

H-, J-, and K-band (rest-frame optical) spectroscopic measurements are incorporated into the sample of galaxies from GOODS-N using MOSDEF (Kriek et al. 2015). MOSDEF is ideal for a sample of low-mass, UV/optically selected galaxies, as the survey is biased toward galaxies in the middle of the SFMS in particular (see Figure 16 in Kriek et al. 2015). However, due to the low signal-to-noise ratio (S/N) continuum of the MOSDEF spectra, this spectroscopy proved unsuitable for direct use in our SED fitting methods. Instead, we utilize spectroscopic redshifts and metallicities measured from MOSDEF spectra by Sanders et al. (2018). This sample contains galaxies with robustly measured redshifts at

$2 \leqslant z \leqslant 2.7$, $\log(M_\star/M_\odot) \geqslant 9$, and high-S/N H$\alpha$ and Hβ measurements. AGN are also excluded from this sample with a combination of IR, X-ray, and emission line diagnostics. Multiple indicators are used to measure the oxygen abundance of each galaxy. Cross-matching via R.A. and decl. to the Sanders et al. (2018) catalog returns our final sample size of 60 galaxies. Oxygen abundances are converted to metallicities using a solar oxygen abundance of $12 + \log(\mathrm{O/H})_\odot = 8.69$ (Asplund et al. 2009).

3. Analysis

In this section, we discuss the methods used to measure the SEDs of resolved subcomponents of galaxies. Galaxies are decomposed into central and outer components with color selections in Section 3.1. In Section 3.2, we discuss the PROSPECTOR code (Johnson et al. 2021) and the various settings and templates used. Sections 3.2.1 and 3.1.1 discuss specific priors and assumptions used in the SED modeling, namely the metallicities and dust-obscured star formation. Last, Section 3.3 includes a description of the iterative method used to estimate the unresolved IRAC photometry of the central and outer components.

3.1. Center and Outskirts Decomposition

In the present Universe, the Milky Way bulge and thick disk are known to be older and redder than the surrounding regions of the galaxy (e.g., Bensby et al. 2017; Barbuy et al. 2018; Miglio et al. 2021; Queiroz et al. 2021), possibly forming at $2 < z < 3$. In particular, Queiroz et al. (2021) detect a population of counter-rotating stars in the Milky Way bar and bulge, which could potentially be remnants of the instability-induced clumpy star formation that helped form the bulge and is observed in star-forming disks at $2 < z < 3$ (Elmegreen et al. 2008; Huertas-Company et al. 2020). As such, a forming stellar core can potentially be identified via its rest-frame optical colors. Using resolved, observed-frame $z_{\mathrm{F850LP}} - H_{\mathrm{F160W}}$ colors, we decompose each galaxy in our sample into separate central and outer components. This specific color is chosen because it spans the 4000 Å break, which is a known age indicator and can help identify older stellar populations (e.g., Kauffmann et al. 2003; Wild et al. 2009). Moreover, the central regions of galaxies can often experience significant dust attenuation in their centers (e.g., Tadaki et al. 2017, 2020; Elbaz et al. 2018; Tacchella et al. 2018; Puglisi et al. 2019, 2021; Franco et al. 2020; Gómez-Guijarro et al. 2022), which in turn would allow us to select dense galactic cores by looking for significantly red regions of galaxies. Thus, we should be able to detect central regions that form in a number of ways, including mechanisms such as accretion of star-forming clumps and central starbursts from mergers or gas accretion.

Image cutouts of each galaxy in both filters and segmentation map cutouts are made with Montage v6.0. Nearby objects are masked, and the centroid in F160W is measured via the center of mass. A series of 50 circular apertures with radii ranging from 1 to 10 pixels (0.″06 to 0.″6) are placed at the centroid, and aperture photometries for both F850LP and F160W are measured. Fixed circular apertures are used because any dense central core at this redshift would likely be small enough to fall within the point-spread function FWHM. We then choose the center aperture that maximizes the color (i.e., contains the reddest flux within). To do this, we impose a condition that chooses a local maximum if the following local minimum (at a larger aperture radius) is less than 0.01 times the local maximum color, and the global maximum otherwise. This prevents overestimation of the center aperture by secondary peaks driven by background flux or contamination from dusty star-forming clumps in the outskirts. An example decomposition is shown in Figure 2 in a color image (F160W/F125W/F850LP for the red, green, and blue filters, respectively), as well as F160W and F850LP individually. The central aperture is shown with a green circle and highlighted by a red point in the inset $z_{\mathrm{F850LP}} - H_{\mathrm{F160W}}$ growth curve. The color images and apertures of all 60 galaxies are shown in Appendix A.

The central apertures determined by this method are then confirmed visually, and in cases where a distinct center is not visually identifiable, we rely on the identification from color selection. As another check, we examine the residuals of best-fit exponential disk models for a subsample of 10 galaxies. Subtracting the exponential disk model from the galaxy should leave behind light from the dense stellar core (or other clumpy regions of star formation, which we discuss later), making the presence of this central feature apparent. This test ensures the color-selected central components correspond to distinct morphological regions of the galaxies. The exponential disk fits are not used to subtract the outskirts' contributions from the centers. Exponential disks are fit to the F160W cutouts of the subsample using GALFIT (Peng et al. 2002, 2010), and the best-fitting model is subtracted from the image cutout. For all galaxies in the subsample, the color-selected center aperture encloses the majority of the residual flux, suggesting that these selections are capturing the dense stellar core. Centers selected for these galaxies have an average radius of $R = 2.46 \pm 0.47$ kpc, compared to an average half-light radius of $R_{\mathrm{eff}} = 2.16 \pm 1.86$ kpc. Fifty-eight percent of the galaxies in the sample have a central size greater than their half-light radius, and the median ratio of the two sizes is $R/R_{\mathrm{eff}} = 1.11$, suggesting the defined centers tend to contain roughly half of the light in a given galaxy.

The center fluxes are then computed via aperture photometry for each HST band. Photometric uncertainties are computed by summing in quadrature the sigma image ($1/\sqrt{w}$, where w is the weight image). The corresponding fluxes for the outskirts are computed by subtracting the center from the total catalog fluxes for each filter. The uncertainties for the outskirts are computed by subtracting the center photometric error from the catalog flux error in quadrature.

As mentioned earlier, these centers also likely include significant contribution from the chemical thick disk. However, we are interested in the formation and evolution of the galactic center as a whole, so investigating the evolution of both these components (bulge and thick disk) is useful in understanding the galaxy formation histories as a whole. Moreover, most quenched galaxies at $z \sim 2$ tend to be fast rotators with large velocity dispersions (Newman et al. 2018), and thus are most likely dominated by chemical thick disks, so understanding the formation of this component as well as the rest of the galactic center might help explain this behavior.

3.1.1. Impact of Dust Attenuation and Obscured Star Formation

One potential contaminant in our central SFHs is dust-obscured star formation. Dust attenuation is known to play a large role in the centers of massive star-forming galaxies and

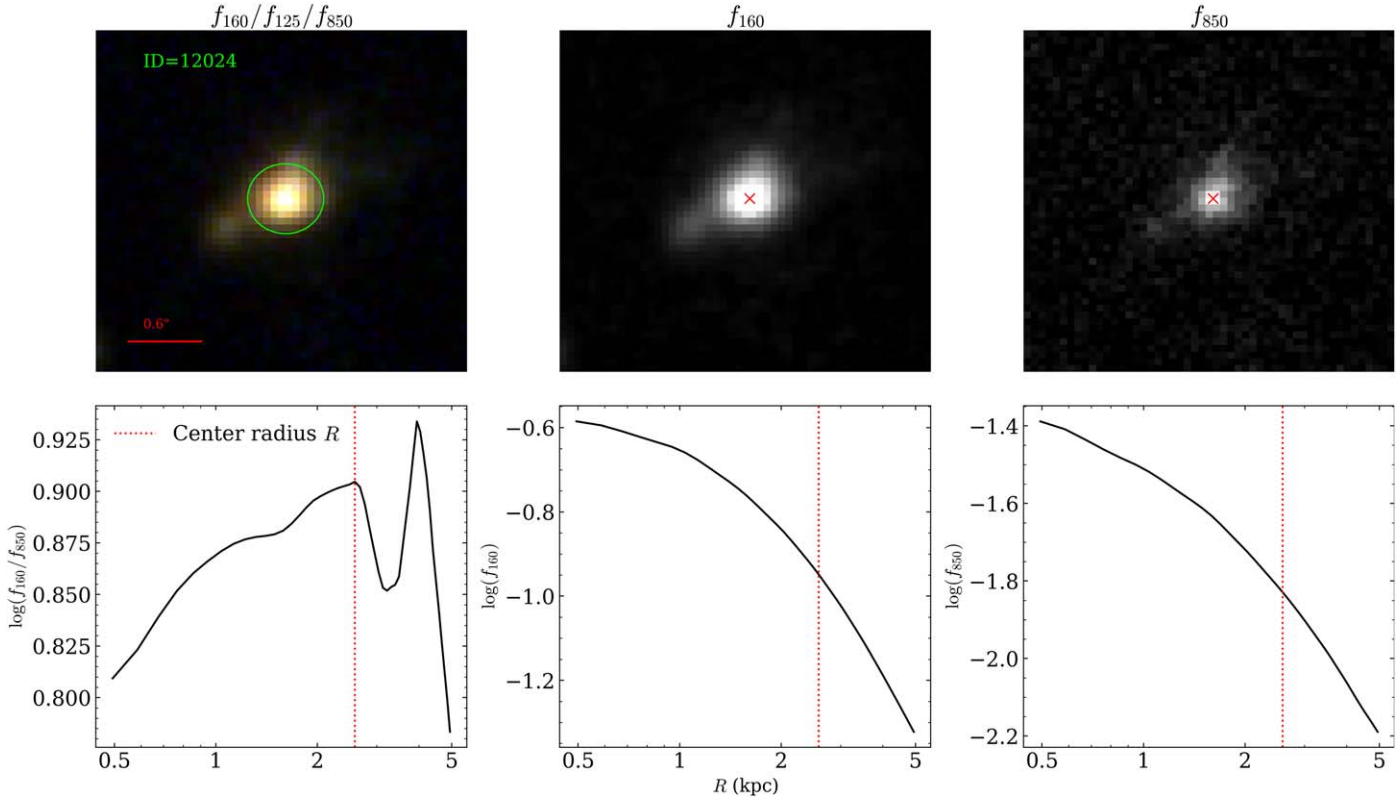

Figure 2. Example central–outer decomposition for a galaxy in our sample. The left column shows the target galaxy in a three-color image: red = F160W, green = F125W, and blue = F850LP. The bottom panel shows the growth curve of the $z_{\rm F850LP} - H_{\rm F160W}$ color (equivalently $\log(f_{\rm F160W}/f_{\rm F850LP})$) with increasing aperture radius R. Apertures are centered on the F160W centroid (red x in middle panel). The selected center aperture is indicated with a green circle in the three-color image and with a dotted red line in the growth curve. The middle and right columns show the F160W and F850LP images of the target galaxy, with corresponding light curves below. Centroids for both filters are shown with red x symbols. The secondary peak in the $z_{\rm F850LP} - H_{\rm F160W}$ color is due to the depth of the F850LP image: because the F850LP imaging is shallower than F160W, enclosing more of the faint outskirts of the galaxy makes the growth curve tend to be redder, even though the intrinsic color might not be changing.

starbursts (e.g., Tadaki et al. 2017, 2020; Elbaz et al. 2018; Tacchella et al. 2018; Puglisi et al. 2019, 2021; Franco et al. 2020; Gómez-Guijarro et al. 2022), and it could potentially contribute significant obscured star formation to the centers of these less-massive galaxies as well. Because our photometry only samples out to the rest-frame NIR ($<2\,\mu$m), the SFHs measured from these SEDs will likely not capture these effects.

To constrain the impact of dust-obscured star formation, we check for far-IR (FIR) counterparts to our galaxies in the GOODS-N "super-deblended" catalog presented in Liu et al. (2018). We find that only three of our sources have significant ($S/N > 1$) flux at 850 μm when cross-matching to FIR sources within $1''$. These FIR measurements are not robust detections ($S/N < 2$), but they will allow us to compute upper limits on the obscured star formation in these galaxies. Using the $S_{850\,\mu{\rm m}} - {\rm SFR}$ conversion for Lyman-break galaxies (see Equation (10) in Webb et al. 2003), we measure an upper limit of $<40\,M_\odot\,{\rm yr}^{-1}$ on the three FIR counterparts, which is much lower than the peak SFRs measured from the integrated galaxy SEDs ($>100\,M_\odot\,{\rm yr}^{-1}$). Moreover, the number of detections is a small fraction of the total sample (5%) and is limited to some of the most massive galaxies in the sample ($\log(M/M_\odot) > 10.8$), which are already known to have more significant contributions from obscured star formation.

The marginal detections (if detections at all) for a small fraction of sample galaxies, the higher mass of these detections with relation to the whole sample, and the relatively low dust-obscured SFRs suggest that optically thick dust obscuration of star formation (i.e., star formation that does not appreciably contribute to the UV/optical SED) does not seem to be a common and substantial contribution to the total SFR budget in the sample considered here.

3.2. PROSPECTOR Inputs

SED fitting is done using the fully Bayesian PROSPECTOR code (Johnson et al. 2021). PROSPECTOR forward models observed data (both spectra and photometry) of composite stellar populations (CSPs) given a set of parameters describing the CSP (e.g., mass formed, metallicity, dust extinction, etc.) and other observational effects (e.g., filters, redshift, etc.), which can either be fixed or varied. Using these models, likelihood and posterior probabilities are computed via comparison to observed data and noise properties. CSPs are generated with Flexible Population Stellar Synthesis (FSPS; Conroy et al. 2009, 2010; Conroy & Gunn 2010) code using PYTHON-FSPS (Foreman-Mackey et al. 2014).

Priors are also important ingredients to PROSPECTOR, given the Bayesian forward-modeling approach this code takes. Because significant parts of SED parameter space can be highly degenerate (e.g., the age–dust–metallicity degeneracy), priors can help shape the posterior distribution and capture more accurate stellar population properties. Moreover, choice of prior is crucial in determining nonparametric (piecewise step function) SFHs with lower-quality data. In a non-Bayesian framework (using regularization), Ocvirk et al. (2006)

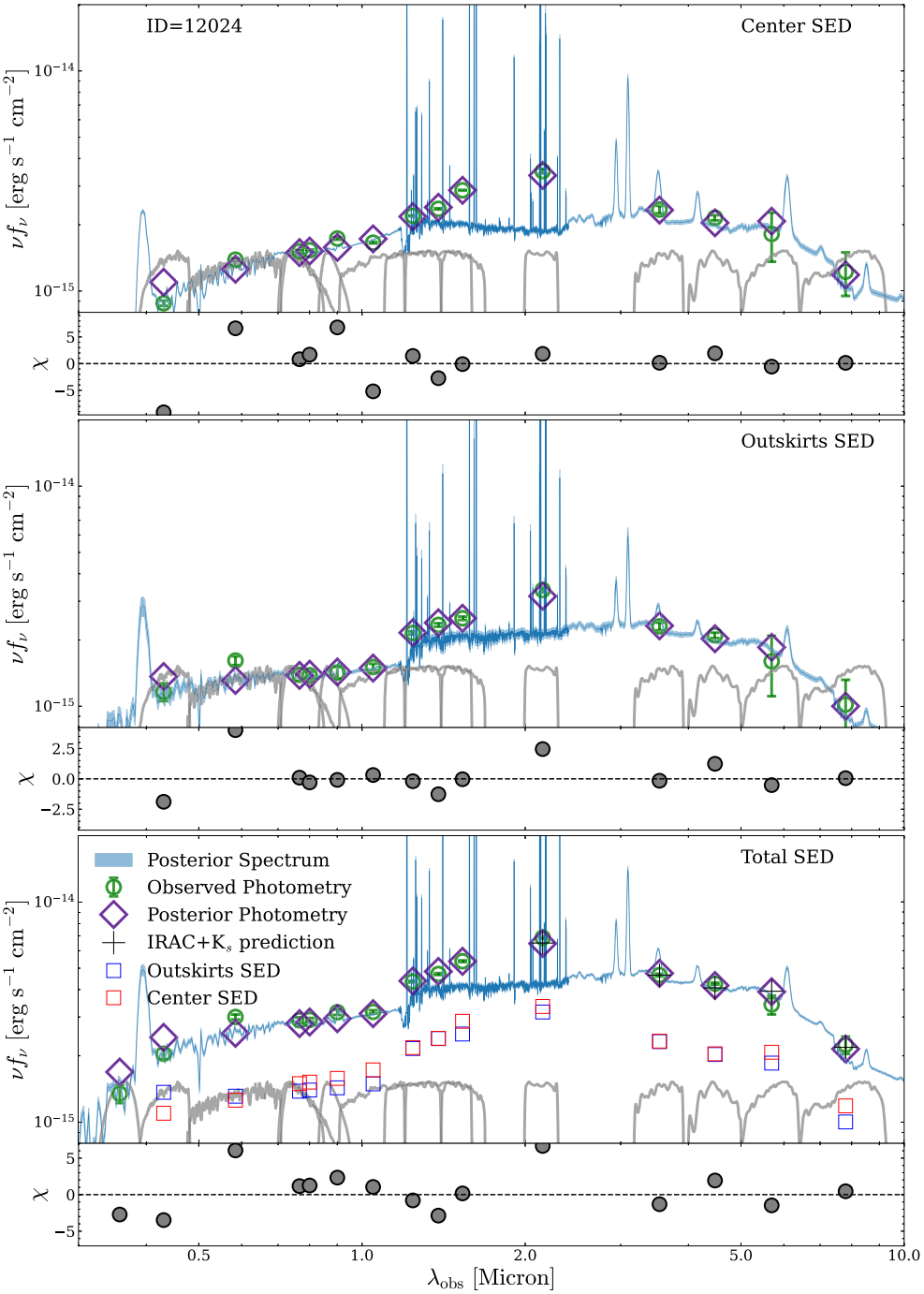

Figure 3. Example SED fits to a galaxy from our sample. The three figures show the SEDs of the center, outskirts, and total galaxy from top to bottom. The top panel in each figure shows the SED, and the bottom shows the uncertainty-normalized residual ($\chi = (f_{\rm obs} - f_{\rm model})/\sigma_{f,\rm obs}$) between the observed and predicted photometry as a function of wavelength. The x-axis of each figure is the observed wavelengths in microns. The blue line is the best-fit spectrum from PROSPECTOR, with the 16−84 percentile range indicated by the shaded region. Best-fit photometry is shown with purple diamonds, and error bars indicate the 16−84 percentile range. Observed photometry and uncertainties (including converged IRAC and K-band data for the center and outskirts) are shown with black and green circles. For comparison, the center and outskirts best-fit photometries are shown with red and blue squares in the bottom figure, and the best-fit IRAC and K-band photometries from both components are added and indicated with black crosses. Gray curves show the transmission for all included filters.

determine that only eight episodes of star formation can be recovered with high-quality spectroscopy ($R = 10{,}000$, S/N = 100). However, Leja et al. (2019) find that with PROSPECTOR, nonparametric SFHs can be useful with photometry or low-quality spectra if the SFH prior is well-tuned.

In this work, the redshift is fixed at the spectroscopic redshift measured from MOSDEF. The metallicity ($\log Z_\star$) is handled with Gaussian priors for SED fits to the total galaxy and both subcomponents. These priors are centered on the median MOSDEF metallicities from Sanders et al. (2018) with widths equal to the 16–84th percentile range from the Sanders et al. (2018) metallicity sample. The Gaussian priors are only applied to the outer component, because we assume that the metallicity of the galaxy should be dominated by the metallicity from the

outskirts. This is supported by the fact that the Milky Way bulge consists of an older, metal-poor population (e.g., Queiroz et al. 2021), and thus centers of star-forming galaxies at $z \sim 2.3$ may be more metal-poor than the rest of the light from the galaxies. We discuss the impact of this metallicity prior on the different components, as well as the robustness of the integrated galaxy SED fit with and without a metallicity prior, in Section 3.2.1 and Appendix C, respectively. Dust and nebular emission are incorporated, with the V-band optical depth ($\tau_V = 1.086 A_V$) and ionization parameter ($U_{\rm neb}$) allowed to vary.

SFHs are modeled nonparametrically using the continuity prior described in Leja et al. (2019). This prior fits directly for the ratio of star formation rates (SFRs) between bins ($\Delta \log(\mathrm{SFR})$), which weights against discontinuities in the SFH (via sharp jumps or drops in the SFR). Each individual ratio ($\log(\mathrm{SFR}_i/\mathrm{SFR}_{i+1})$) is drawn from a Student's t-distribution, as in Leja et al. (2019), with an initial value of $\log(\mathrm{SFR}_i/\mathrm{SFR}_{i+1}) = 0$ for all SFR bins i. The SFH is computed over seven fixed age bins (in lookback time from the observed redshift):

$$\begin{aligned} 0 < t < 30\ \mathrm{Myr} \\ 30 < t < 99\ \mathrm{Myr} \\ 99 < t < 218\ \mathrm{Myr} \\ 218 < t < 479\ \mathrm{Myr} \\ 479\ \mathrm{Myr} < t < 1.06\ \mathrm{Gyr} \\ 1.06 < t < 2.32\ \mathrm{Gyr} \\ 2.32 < t < \sim 2.7\ \mathrm{Gyr}, \end{aligned} \quad (1)$$

where the last bin is adjusted to account for the age of the universe at the observed redshift. Only five age bins are used when decomposing the IRAC and K-band photometry, as discussed in the next section. The smaller size of the oldest bin also allows for a maximally old population (see Leja et al. 2019). The total mass formed in the best-fit SFH (M_F) is left as a free parameter, and an initial guess is taken from the CANDELS/SHARDS measurements from FAST (Barro et al. 2019). For subcomponents, this initial guess is scaled by the fraction of light in F160W:

$$M_x = M_{\rm tot}\left(\frac{f_{\mathrm{F160W},x}}{f_{\mathrm{F160W,tot}}}\right), \quad (2)$$

where x refers to either the central or outer component. The mass-weighted age (t_M or $\langle t_\star \rangle_M$) is determined from the total mass formed and the SFH, and the total mass formed is corrected to a stellar mass ($M_\star$) using the approximation

$$\log M_\star = \log M_F + 1.06 - 0.24 \log(t_M) + 0.01 \log(t_M)^2\,, \quad (3)$$

with masses in solar units and ages in years (Leja et al. 2013, Equation (2)). This mass accounts for the total mass in stars and stellar remnants at observation (i.e., excluding mass lost during supernovae, winds, etc.), rather than all the mass formed throughout the galaxy's history.

SEDs are fit to all filters described in Section 2.1 where available for the total galaxy. The U-band is not fit for subcomponents, because it cannot be resolved (the unresolved K-band and IRAC data are dealt with in an iterative process

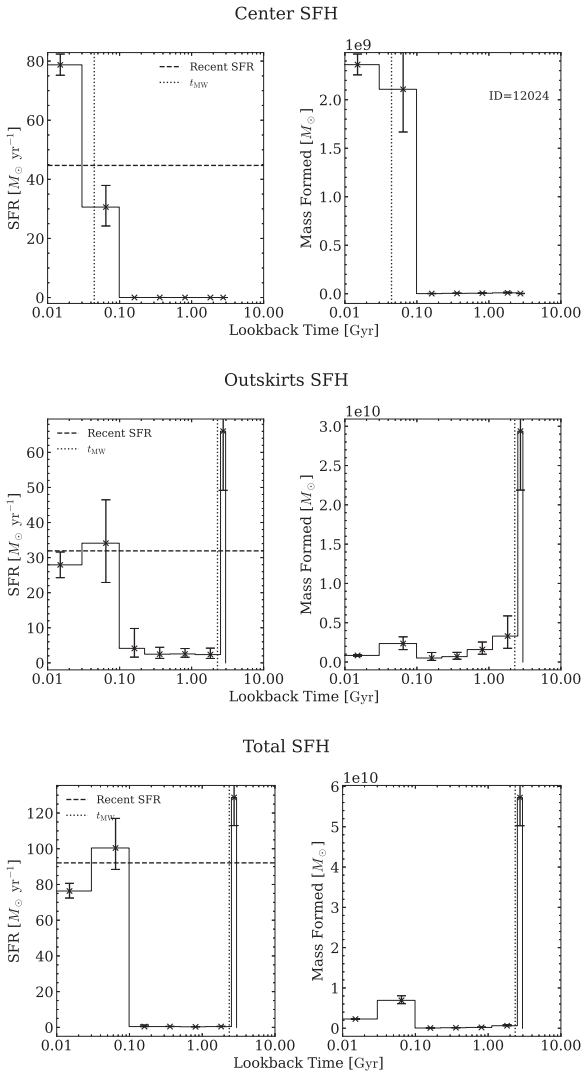

Figure 4. Example best-fit SFHs for a galaxy from our sample. The three figures show the SFHs for the center, outskirts, and total galaxy from top to bottom. For each figure, the left and right panels show the SFR and mass formed in each age bin as a function of lookback time from observation (i.e., a lookback time of 0 Gyr is the galaxy at the observed redshift). The error bar in each age bin shows the 16−84 percentile range. The dotted and dashed lines show the mass-weighted ages and recent (past 100 Myr) SFRs for the two subcomponents and the total galaxy.

explained in Section 3.3). Best-fit parameters are first determined by pure maximum-likelihood estimation via the Levenberg–Marquardt (LM). method. Because much of the likelihood space in SED fitting is non-Gaussian and ill-conditioned, optimization methods like LM are not recommended for actually determining parameter values (Johnson et al. 2021). Instead, the LM-determined parameters are used as an initial guess for Monte Carlo sampling of the posterior probability distribution function (PDF). Monte Carlo sampling is done using Monte Carlo Markov Chains (MCMC) in the EMCEE code (Foreman-Mackey et al. 2013) with 64 walkers and 256 iterations (32 and 128 when decomposing IRAC photometry, see Section 3.3). Best-fit parameters are then determined by finding the maximum a posteriori (MAP) sample with uncertainties from the 16th and 84th percentiles of the chain. Example PROSPECTOR results for the total galaxy as well as center and outskirts components are shown in Figures 3 (SEDs) and 4 (SFHs) and in Appendix B (covariances). For this

example, the SFHs of the outskirts and total galaxy show two distinct peaks of star formation, compared to the single peak in the center. These peaks, combined with the potential tidal features visible in the F160W and F850LP images of the galaxy (Figure 2), suggest this galaxy may have undergone a recent merger, resulting in the increase in star formation in the outskirts. A merger could also have caused the burst of star formation in the center, since mergers may play a significant role in central star formation by driving gas to the center of galaxies (e.g., Puglisi et al. 2019, 2021).

3.2.1. Impact of Adopted Assumptions of Metallicity Priors

Global metallicity measurements from Sanders et al. (2018) are used as priors in the SED fitting. Because these measurements are derived from the integrated spectrum, using them as priors for the resolved components requires specific assumptions. In the previous section, we describe how the metallicity prior is applied to both subcomponents equally. Because the metallicities are derived from spectra of the whole galaxy, they should be representative of the metallicities of both subcomponents as well. Moreover, the majority of metallicity gradients in star-forming galaxies are flat at $z \sim 2$ (Simons et al. 2021), so there should not be significant differences between the center and outskirts metallicities. On the other hand, the centers of galaxies in this sample are brighter and larger than the outskirts on average, and slit losses should affect the outskirts more significantly than the centers. As such, the metallicity measurements would then tend to be better priors for the centers as opposed to the outskirts. To test the effect of various metallicity prior prescriptions, we rerun the entire sample with three test runs: applying the Sanders et al. (2018) metallicity prior to the outskirts and not the center, applying the prior to the center and not the outskirts, and applying the prior to neither subcomponent. For the component (s) without the Sanders et al. (2018) metallicity prior, we apply a top-hat prior ranging from $-3 < \log(Z/Z_{\odot}) < 0.2$. These test runs are compared to the "primary" run (Sanders et al. 2018 metallicity prior applied to both components), and the resulting impact on the SFHs is shown in Figure 5. Applying different priors prescriptions has no significant effect on the SFHs on average for any of the test runs, and the 16−84 percentile range is small ($<5\,M_{\odot}\,\mathrm{yr}^{-1}$). While the 5−95 percentile range is larger, especially for certain time bins, it is still $<40\,M_{\odot}\,\mathrm{yr}^{-1}$, significantly less than the peak SFRs measured ($>100\,M_{\odot}\,\mathrm{yr}^{-1}$). Thus, we consider the results where the Sanders et al. (2018) metallicity prior is applied to both subcomponents, as in the original procedure.

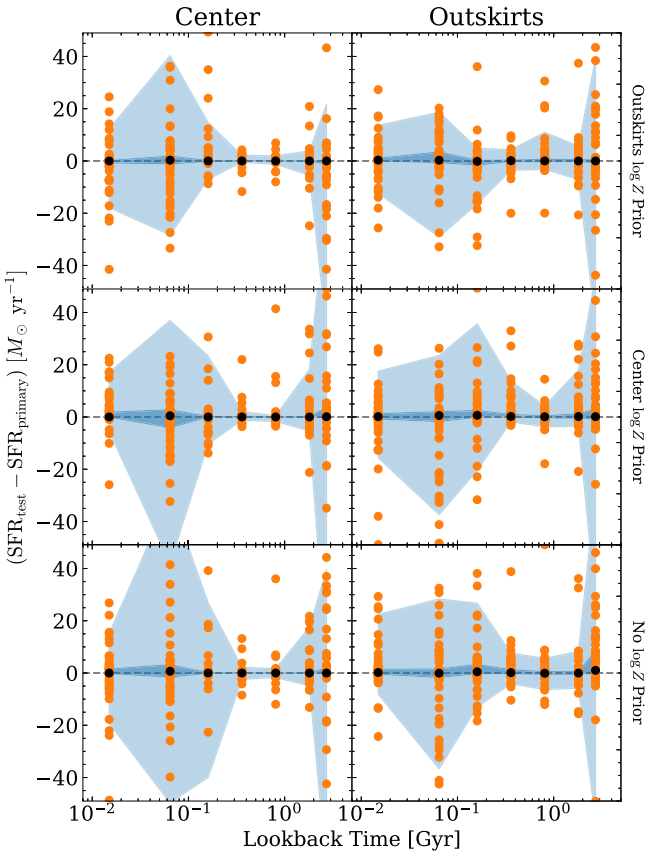

Figure 5. Comparison of star formation histories for different metallicity prior test runs to the primary run. The resulting SFHs from SED fitting are robust to the choice of metallicity prior. For the primary run, Gaussian priors based on the Sanders et al. (2018) metallicity measurements are applied to both components. For the three test runs, the Sanders et al. (2018) metallicity priors are applied to the outskirts only (top row), the center only (middle row), and neither subcomponent (bottom row). Orange points indicated the difference in the SFH between the test and primary runs at each time bin. Black points show the median SFH difference, and light and dark blue shaded regions indicate the 16%−84% and 5%−95% percentile ranges, respectively.

3.3. Iterative Method for Decomposed IRAC Photometry

The resolution of HST imaging allows for direct measurements of the decomposed center and outskirts fluxes. However, data from other instruments, namely ground-based *K*-band from Subaru/MOIRCS and four MIR bands from Spitzer/IRAC, are too low-resolution for resolved measurements. While fitting only to the HST photometry is possible, the constraints provided by the observed NIR/MIR are crucial in measuring the stellar mass and age, because this wavelength regime traces the rest-frame optical and NIR at $z \sim 2.3$. In order to incorporate these important filters into the decomposed SEDs, we use a simple iterative method to estimate the *K*-band and IRAC flux of both the center and outskirts. This also motivates our use of a simple two-component decomposition in lieu of more complicated techniques (e.g., Voronoi tesselation, as in Fetherolf et al. 2020), as the system of equations becomes more difficult to solve with more components. It should be noted that the *U*-band photometry is excluded from the decomposed components and this iterative method.

The goal of this scaling is to use the shape of the HST-only SED to estimate initial *K*-band/IRAC SED, as well as the relative contribution of the total *K*-band/IRAC photometry to each component, and to iteratively apply these estimated fluxes to future resolved SED fits. This process utilizes the resolved information from the HST photometry as well as constraints from the total *K*-band/IRAC fluxes. First, SEDs are fit using fewer walkers and iterations (32 and 128, respectively) to the HST filters only (the number of SFH bins is reduced to five for this step, so the number of data points is greater than the number of free parameters) in order to get MAP photometry estimates for all HST filters as well as the *K*-/IRAC bands. We then define the corrected *K*-band/IRAC photometry as the MAP-predicted photometry multiplied by the ratio of the observed to MAP F160W flux (the longest-wavelength HST

filter available):

$$f_{x,\mathrm{corr}}(\lambda) = f_{x,\mathrm{MAP}}(\lambda)\left(\frac{f_{x,\mathrm{obs}}(\mathrm{F160W})}{f_{x,\mathrm{MAP}}(\mathrm{F160W})}\right), \quad (4)$$

where λ refers to one of the K-band or IRAC filters and x indicates the center or outskirts subcomponent. The "MAP" and "obs" labels indicate these are fluxes estimated by PROSPECTOR or observed photometries, respectively. This first scaling ensures the estimated K-band/IRAC fluxes are consistent with the observed flux of the longest resolve wavelength, as significant residuals between the observed and predicted F160W flux could result in an incorrect correction to the total K-band/IRAC flux and increase the number of iterations needed for convergence.

The corrected K-band/IRAC fluxes are then scaled to agree with the observed K-band/IRAC fluxes of the total galaxy:

$$f'_x(\lambda) = f_{x,\mathrm{corr}}(\lambda)\left(\frac{f_{\mathrm{obs}}(\lambda)}{\sum_x f_{x,\mathrm{corr}}(\lambda)}\right), \quad (5)$$

where the summation is over the center and outskirts components and $f'_x(\lambda)$ is the "observed" flux of the subcomponents to be fit in the next iteration. The uncertainty in these "observed" fluxes is given by

$$\delta f'_x(\lambda) = \delta f_{\mathrm{obs}}(\lambda)\sqrt{\frac{f_{\mathrm{obs}}(\lambda)}{f_{x,\mathrm{corr}}(\lambda)}}. \quad (6)$$

This step matches the estimated K-band/IRAC flux of the total galaxy via the SED fits to the two components to the observed flux. By doing this, the shape of the IR SED, as inferred by the HST-only fit, is combined with the correct normalization to observed IR photometry.

The SED is then fit again, this time including the "observed" center and outskirts photometries and uncertainties. The process is repeated until the estimated total K-band/IRAC flux changes by <5% in all but one filter (this allows for flexibility when dealing with bands with very large photometric errors). This convergence is generally quick, though due to the longer computational times required to run PROSPECTOR, we limit this method to a maximum of 10 iterations. Only 2 of the 60 galaxies reach this limit. The behavior of the fractional change in the total K-band/IRAC flux over 10 iterations is show in Figure 6 (solid lines and points) and compared to the fractional photometric error in each band (dashed lines). After four iterations, all bands are below the 5% threshold for the change in flux. At the same times, all bands except for the K-band have changed by less than the corresponding fractional error, indicating that further refining the photometry in future iterations is unnecessary.

Finally, PROSPECTOR is run with the full number of walkers, iterations, and SFH bins (64, 256, and 7, respectively) on the components using these converged values for the K-band/IRAC flux. The summed center and outskirts photometries in the NIR and MIR are shown with black crosses in Figure 3. In general, there is good agreement between the observed K-band/IRAC flux of the total galaxy and the predicted photometry from this iterative analysis. As mentioned before, including rest-frame optical/NIR is crucial in constraining the age, stellar mass, and SFH of the galaxy (e.g., Papovich et al. 2001, 2004; Pforr et al. 2012, 2013; Conroy 2013; Mobasher et al. 2015). Moreover,

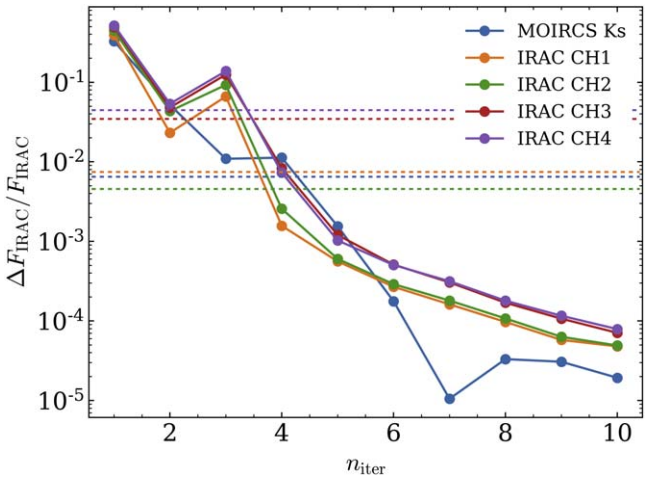

Figure 6. Convergence of the decomposed photometry in the Subaru/MOIRCS K-band and Spitzer/IRAC channels for the example galaxy from Figures 3, 4, and Appendix B. The fractional change in the summed (i.e., $\sum_x f_{x,\mathrm{corr}}$) K-band/IRAC photometry is compared to the iteration number, and it shows that after four iterations the behavior in all but one band is consistent. Dashed lines indicate the fractional error in each band for the example galaxy. After four iterations, the fractional change in the flux is less than the error in the flux for all IRAC bands.

fitting our sample with resolved photometry only results in stellar masses and metallicities that differ from fits including K-band/IRAC by >0.2 dex, while the mass-weighted ages and recent SFRs can differ by $>20\,M_\odot\,\mathrm{yr}^{-1}$ and >1 Gyr, respectively. As such, including the unresolved K-band/IRAC photometry is crucial in our analysis.

4. Star Formation Histories

The measured central SFHs of our sample may provide insight into how dense stellar centers in Milky Way progenitors may have formed. If centers in these lower-mass systems formed first, followed by inside-out growth of the surrounding regions (e.g., Carrasco et al. 2010; van Dokkum et al. 2010; Nelson et al. 2016), then we would expect to see significant levels of star formation early on. In the cold-mode accretion/clump merger scenario (Dekel et al. 2009a) or other scenarios where the center grows in a coeval way with the rest of the galaxy (e.g., Kormendy & Kennicutt 2004), star formation rates should be more constant and the SFH should have a shape similar to that of the outskirts, though an increase in the clump accretion rate (e.g., van Dokkum et al. 2013) could result in a sharp peak in the bulge SFH. Similarly, a burst of star formation could imply a rapid growth of the center via wet disk contraction (Dekel & Burkert 2014; Zolotov et al. 2015; Tacchella et al. 2018) and the galaxies with the strongest bursts of star formation should appear the most compact.

Figure 7 shows the SFHs (sSFR and fraction of mass formed) of the center (top), outskirts (middle), and total galaxy (bottom) for all 60 galaxies in the sample. The shading indicates how many galaxies have a similar SFR in a given age bin. One prominent feature is a strong burst of star formation between lookback times 30 and 100 Myr before $z \sim 2.3$. This indicates that centers in these galaxies are younger and have not built slowly over time. For most of the galaxies, both the outskirts and total galaxy build up more of their mass earlier on than the center, and all three show a quenching event 0–10 Myr before observation. This quenching event agrees with results that suggest bulge formation can morphologically quench

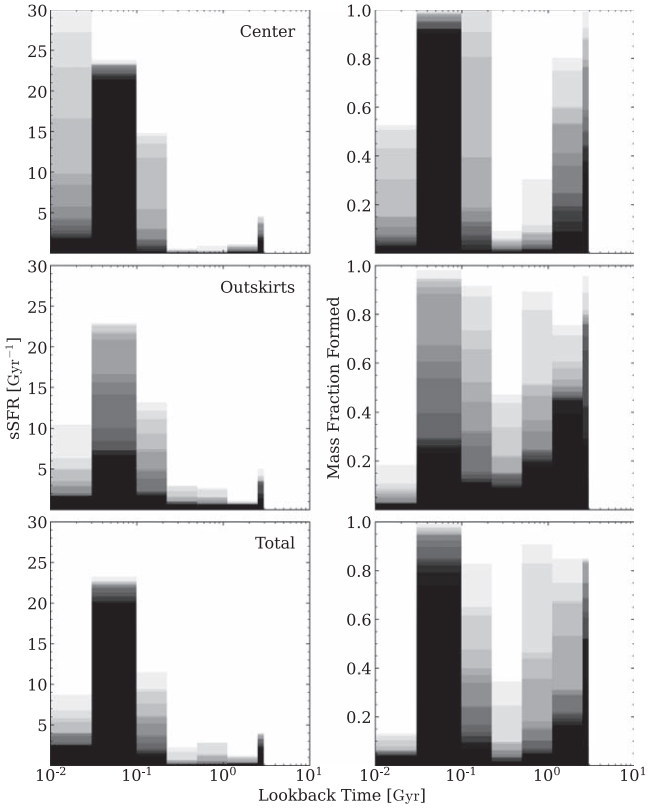

Figure 7. Center SFHs show a strong, recent burst of star formation. SFHs for the center (top) and outskirts (middle) components, as well as the total galaxy (bottom), are shown for all 60 galaxies in the sample. Specific SFRs (sSFR = SFR/$M_\star$) are shown in the left column, and the fraction of mass formed (mass formed in an age bin divided by total mass formed) is shown on the right. Darker regions indicate a higher density of galaxies. The lookback time is relative to the redshift of observation (i.e., a lookback time of 1 Gyr refers to an epoch 1 Gyr earlier than $z \sim 2.3$).

galaxies by stabilizing the disk against future star formation (Martig et al. 2009) or that rapid gas consumption/AGN fueling can temporarily suppress star formation after compaction (Tacchella et al. 2016).

In Figure 8, we show the same SFHs, now as individual SFRs, separated in rows by the total stellar mass of the galaxy. This highlights the diversity of the SFHs in this sample. A strong burst of SFR in the center is more prominent in lower-mass galaxies, which also show relatively constant SFR in the outskirts and a rising SFH for the integrated galaxy. At higher masses, a single burst of star formation in the center is less common, with higher star formation rates usually distributed over a wider range of lookback times. The total SFR in these galaxies is also higher and more constant in these galaxies, compared to the increasing total SFHs in lower-mass galaxies. This suggests that these galaxies may be undergoing inside-out growth (Carrasco et al. 2010; van Dokkum et al. 2010, 2014; Nelson et al. 2016), forming a larger fraction of the center mass at earlier times.

Figure 8 also illustrates the difference between the SFHs of the centers and outskirts of these galaxies. In most of the sample, the center exhibits a large burst in star formation at late times, while the outskirts form stars more steadily and have higher SFRs in general. This highlights the differential formation histories of the inner and outer regions of star-forming galaxies and establishes the existence of a formation pathway distinct from the canonical inside-out growth mechanism used for massive galaxy formation.

4.1. On the Robustness of the Reconstruction of the SFH

The robustness of the reconstruction of the SFH in nonparametric form made by PROSPECTOR has been extensively tested in a number of previous work (Johnson et al. 2021; Ji & Giavalisco 2022; Leja et al. 2022; Tacchella et al. 2022). In particular, these works have used synthetic galaxies from the IllustrisTNG cosmological hydrodynamical simulations (Marinacci et al. 2018; Naiman et al. 2018; Nelson et al. 2018, 2019a; Pillepich et al. 2018, 2019; Springel et al. 2018) to directly compare the PROSPECTOR SFH output to the input galaxies' SFHs. They have also tested the stability of the results against assumed priors—in particular, priors on the time dependence of the discretized SFH itself (e.g., continuity versus Dirichlet priors). The general conclusions from these works is that the nonparametric SFHs derived by PROSPECTOR are robust and stable when good-quality photometry covering a broad range of the rest-frame SED from UV to near-IR, such as ours, is available, and when some parameters, such as spectroscopic redshift and metallicity, are independently known and not left as free parameters during the fitting procedure. Here, although we do not repeat their tests and follow them in adopting the continuity prior when deriving the SFH, we do test the stability of our results against the input photometry, the time binning adopted for the SFH reconstruction, and the adoption of the metallicity prior. In Appendix C, we have compared the SFHs of the integrated galaxies shown in Figure 8 with SFH measurements obtained from a much expanded photometric data set that comprises 42 photometric bands with different time binning (nine time bins versus our adopted seven bins) and with and without assuming a strong metallicity prior. As discussed in Appendix C, we conduct our test for the integrated SFHs only and not for the centers and outskirts as well, because the extended photometric data are derived from ground-based images in natural seeing. The complexity of such a data set, therefore, prevents us from running our decomposition analysis in a robust way in this case. The conclusion from our test is that the integrated SFH is robust and stable, however, which adds strong support that the decomposed SFHs of centers and outskirts, obtained with the same data sets, PROSPECTOR settings, and priors, are robust as well.

4.2. Star Formation Timescales

To further illustrate the different formation histories of galactic centers and outskirts, we compare various star formation timescales for the two components. In particular, we compute two values: the total galaxy timescale (equivalent to twice the standard deviation of the SFH) via

$$\tau_{\rm tot} = 2 \int_{t_{\rm obs}}^{t_{\rm univ}} (t - t_{\rm age})^2 \frac{\rm SFR(t)}{M_{\star,\rm tot}} dt, \quad (7)$$

and the skewness of the SFH

$$\rm Skew = \frac{8}{\tau_{\rm tot}^3} \int_{t_{\rm obs}}^{t_{\rm univ}} (t - t_{\rm age})^3 \frac{\rm SFR(t)}{M_{\star,\rm tot}} dt. \quad (8)$$

The total timescale describes how concentrated the star formation activity in the galaxy is, where a short timescale indicates the star formation is concentrated to a single burst,

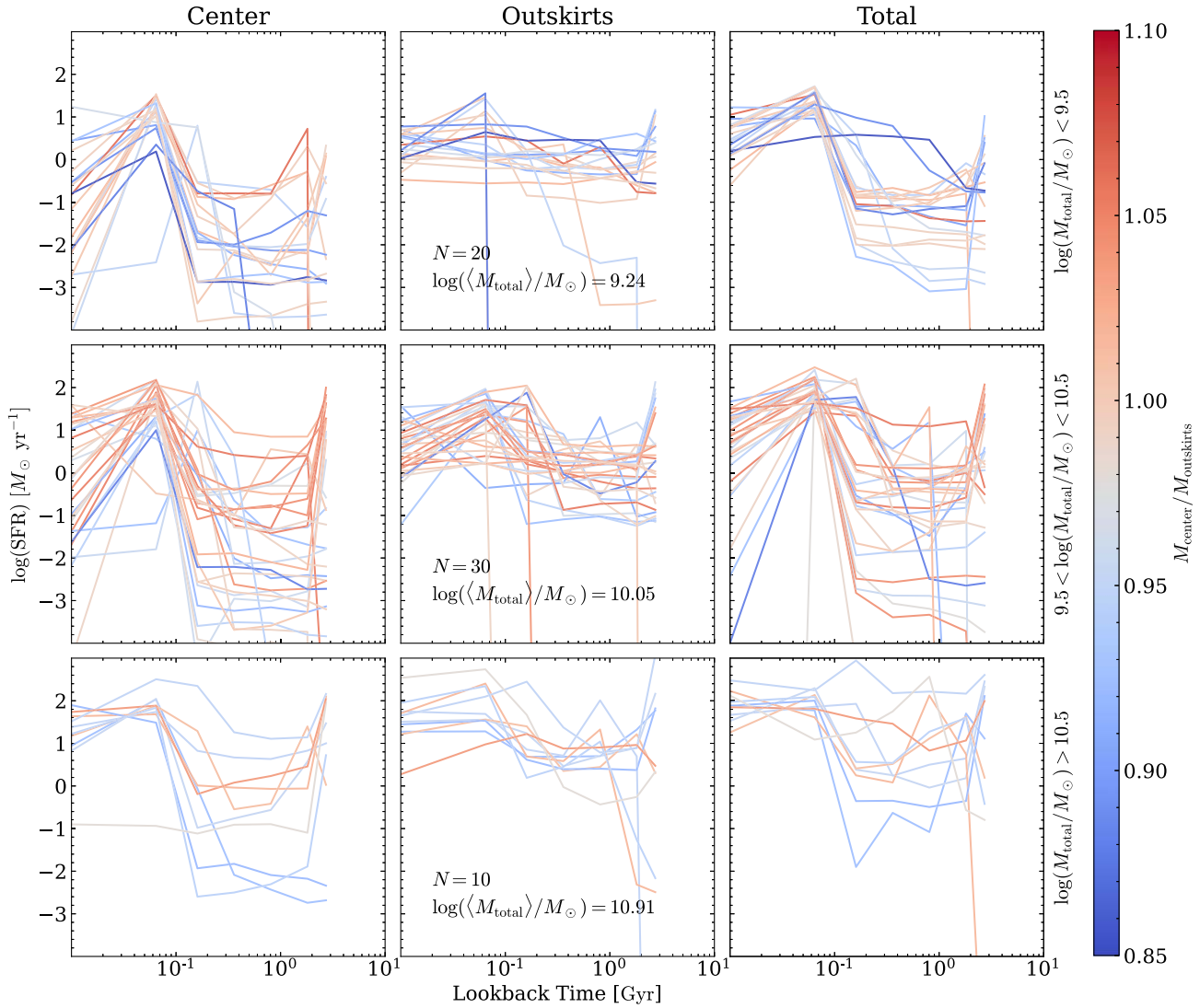

Figure 8. Individual SFHs for all galaxies in the sample, binned by total stellar mass. There is a wide variety of SFHs for these galaxies and their subcomponents. The color indicates the center-to-outer mass ratio. From left to right, the columns show central, outer, and total galaxy SFRs as a function of lookback time from $z \sim 2.3$. The rows show SFHs for galaxies in one of three mass bins: $\log(M_\star/M_\odot) < 9.5$ (low mass, top), $9.5 < \log(M_\star/M_\odot) < 10.5$ (intermediate mass, middle), $\log(M_\star/M_\odot) > 10.5$ (high mass, bottom). For each mass bin, the number and mean mass of galaxies in the bin is shown in the second column.

while a long timescale would represent gradual, continuous build-up of stellar mass. The skewness describes how late or early the star formation is occurring, with a large positive skewness indicating the star formation occurs late in the galaxy's history, while a large negative skewness indicates significant early star formation. Conversely, a skewness near zero implies the star formation rate is evenly distributed throughout the galaxy's history.

In Figure 9, we compare the skewness of galaxy centers (circles) and outskirts (squares) over a range of total stellar masses, also including a third parameter in the total timescale ($\tau_{\rm tot}$). Generally, galaxy centers have a large positive skewness, indicating most of the star formation in the core occurs at later times. Conversely, the outskirts have low skewness for all masses. The difference between the inner (red) and outer (blue) regions is also apparent in the inset histogram. The short timescales on which this star formation occurs in the cores is also indicative of a late burst of star formation, which is reflected in the SFHs in Figures 7 and 8. Conversely, the outskirts appear to form in much more gradual fashion, assembling their stellar mass over longer times, crudely $\approx 5\times$ longer than the center, with slowly increasing SFR. Notably, the skewness of the centers decreases on average with increasing mass (red, open circles) while that of the outskirts stays constant (blue, open squares), further suggesting that higher-mass star-forming galaxies in the sample have a different central formation history than their low-mass counterparts.

4.3. Recent Star Formation and Compaction

The SFH of the centers often shows large enhancements of SFR in the two most recent time bins at 10 and 100 Myr, indicative of a burst, during which time they form a substantial fraction of their stellar mass (72% on average). During the same time period, for most galaxies the SFR of the outskirts remains approximately constant and their stellar masses increase substantially less, by only 16%. In other words, in most galaxies the centers become proportionally more massive

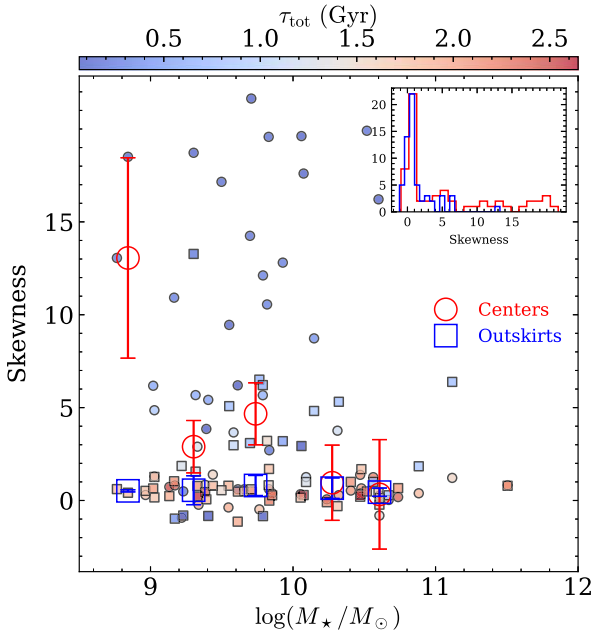

Figure 9. The centers of star-forming galaxies form most of their stars late in a short burst when compared with their outer regions. Circular points indicate the skewness (computed using Equation (8)) of the centers of galaxies, and square points represent the outskirts. The masses shown comprise the total stellar mass of the galaxy. Points are colored based on the total timescale (τ_{tot}, Equation (7)). Red and blue open points indicate the running median for the centers and outskirts, respectively, with error bars showing the standard error in the mean. The inset shows histograms of the skewness for the centers (red) and outskirts (blue) of all galaxies in the sample.

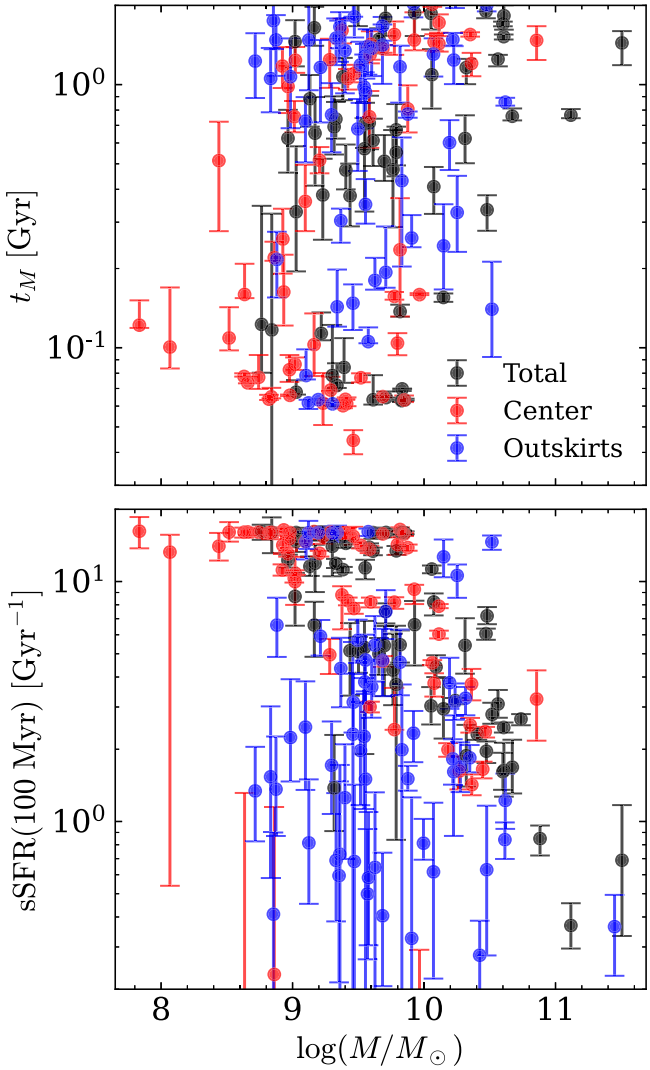

Figure 10. The ages and sSFRs of galaxies in the sample decrease with increasing stellar mass. The mass-weighted ages (top) and sSFRs in the most recent 100 Myr (bottom) are compared to the masses for the center (red), outskirts (blue), and total galaxy (black).

than the outskirts, with an increased mass growth rate of 450% over the center, and thus they become more compact. This is consistent with the general features of the"compaction" phenomenon predicted, for example, in the presence of dissipative gas accretion in unstable disks (e.g., Dekel & Burkert 2014; Zolotov et al. 2015; Tacchella et al. 2016, 2018).

To further examine the possibility that we are observing the centers of our galaxies during a compaction event, we compare the mass-weighted age and sSFR in the most recent 100 Myr, with stellar mass, size r_e, and projected stellar mass density within 1 kpc (Σ_1; see Equation (3) in Barro et al. 2017), used as measures of compactness, in Figures 10 and 11. In Figure 10, we compare the mass-weighted age (top) and recent sSFR (bottom) with the mass of the center (red), outskirts (blue), and total galaxy (black). For the majority of galaxies, the centers are indeed substantially younger than the outskirts, with the ages of the integrated galaxies being intermediate. The sSFR mirrors this behavior, with the centers having the largest values and the outskirts the lowest. More massive galaxies also tend to have lower sSFR in the past 100 Myr and their stellar populations are older, in both centers and outskirts, as well as for the integrated system.

In Figure 11, the left and right columns compare the age and sSFR to the size and central density Σ_1 (see Barro et al. 2017; Lee et al. 2018) of the integrated systems, respectively, with both quantities acting as proxies of the compactness. Galaxies are separated into three different bins of total stellar mass, each indicated by different symbols: diamonds for low mass ($\log(M_\star/M_\odot) < 9.5$), pentagons for intermediate mass ($9.5 < \log(M_\star/M_\odot) < 10.5$), and squares for high mass ($\log(M_\star/M_\odot) > 10.5$). The color of a galaxy indicates its α, where $\alpha \equiv \mathrm{SFR}(100\,\mathrm{Myr}) - \mathrm{SFR}(10\,\mathrm{Myr})$. A larger value of α reflects a greater decrease in the sSFR, i.e., the onset of a decrease in SFR that potentially leads to quenching, while a smaller α shows little change in the sSFR (or an increase if $\alpha < 0$). Although there is considerable scatter in these plots, some trends seem discernible.

The top left panel of Figure 11 does not show any overall correlation between stellar age and size. Because such correlation has been observed for quiescent galaxies (Fagioli et al. 2016; Williams et al. 2017; Ji & Giavalisco 2022), this would suggest that these galaxies are not close to initiating the quenching phase. However, the color-coding suggests that the galaxies for which α is larger, i.e., those for which the SFR in the most recent time bin is smaller than in the previous bin, have younger stellar populations, which would be consistent with a bursty behavior. The bottom left panel shows that galaxies with large α are at the top of the sSFR distribution and span the full range of observed size, which would be expected for bursty systems that have not yet started the structural transformations that appear to accompany the quenching process. We note that galaxies with low α seem to preferentially populate the low-sSFR and large-size region of

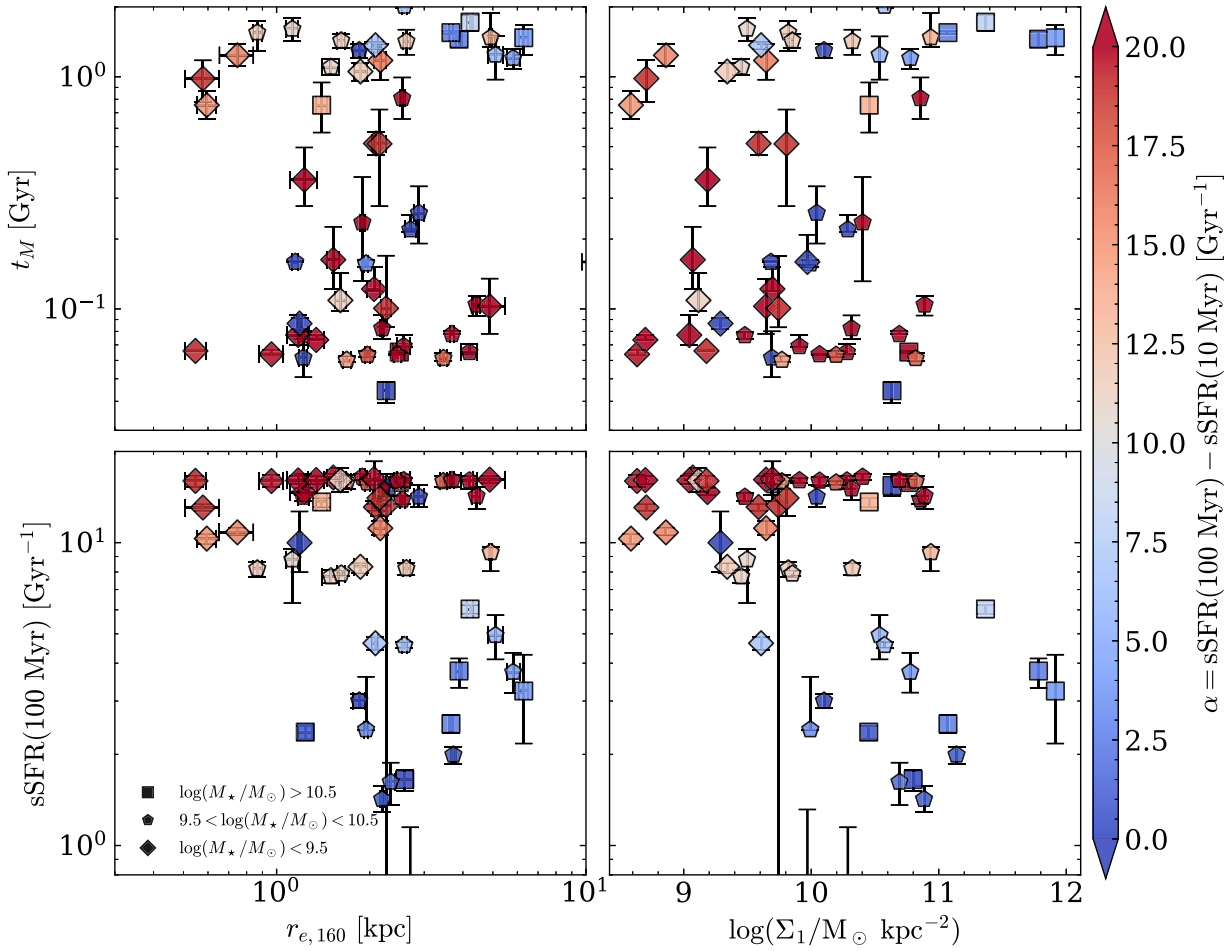

Figure 11. The lack of trends with size suggests that the build-up of the galaxy center does not lead to a significant compaction of the galaxy. The mass-weighted ages (top row) and sSFRs in the most recent 100 Myr (bottom row) in the galaxy center are compared to the half-light radius of the total galaxy (left column) and Σ_1 (right column). In the middle and left columns, symbols indicate galaxies fall in one of three mass bins: diamonds for low mass ($\log(M_\star/M_\odot) < 9.5$), pentagons for intermediate mass ($9.5 < \log(M_\star/M_\odot) < 10.5$), and squares for high mass ($\log(M_\star/M_\odot) > 10.5$). Points in these columns are color-coded according to the differences in their sSFRs at 100 and 10 Myr prior to observation, denoted by α. A higher value indicates the sSFR has decreased more during this period, while a lower value indicates the sSFR has remained relatively constant (or increased, if negative).

the plot. Both the bottom left and bottom right panels show a decrease of sSFR with increasing size and density, respectively. This is likely a mass effect, as more massive galaxies intrinsically have denser centers (e.g., Tacchella et al. 2017), are larger (due to the size–mass relation), and have lower sSFRs for a given SFR (because $\mathrm{sSFR} \propto M_\odot^{-1}$). The top right panel does not appear to contain any trend.

Thus, the question of whether the bursts of star formation that occurred in the centers during the ∼100 Myr prior to observation does or does not result in more compact galaxies, as expected during a gas compaction event (Dekel & Burkert 2014; Zolotov et al. 2015; Tacchella et al. 2016, 2018) or merging of star-forming clumps (Dekel et al. 2009a; van Dokkum et al. 2013), cannot be answered by this analysis. Compaction may still result in the increased SFRs and build-up of a dense and compact central structure in our sample, but our analysis simply does not provide any evidence in favor or against it, even if we do appear to systematically detect bursting centers surrounded by more steadily star-forming outskirts. Finally, we also note that more massive galaxies also tend to be older and experience less of a drop-off in sSFR after the increased star formation levels. As evidenced by Figure 8, these galaxies may be members of a more massive population (compared to the majority of our galaxies that occupy the middle of the SFMS). These galaxies may exhibit inside-out growth and quenching (Carrasco et al. 2010; van Dokkum et al. 2010, 2014), though there is also evidence for outside-in growth (Tadaki et al. 2017, 2020).

4.4. Main-sequence Evolution

From the SFH, we can also predict the evolutionary paths of our galaxies in the SFR versus M_* plane, as well as their position relative to the main sequence. This is done in Figure 12, which shows the evolution of our sample galaxies over the last two SFH time bins. Most galaxies appear slightly above the SFMS (red shaded region) at 100 Myr prior to observation (green points), consistent with being caught during a substantial burst of star formation. Subsequently, in the next time bin, as the burst subsides, they evolve onto the main sequence (yellow points). The majority of galaxies in the sample are also found on the SFMS close to observation (10 Myr bin). This behavior is similar to the confinement of galaxies in the SFMS shown in Tacchella et al. (2016). During the so-called "blue nugget" (compact, star-forming) phase, galaxies move up to the top of the main sequence as SFRs increase, which is seen in the 100 Myr SFRs. Tacchella et al. (2016) find that this is followed by movement down to the

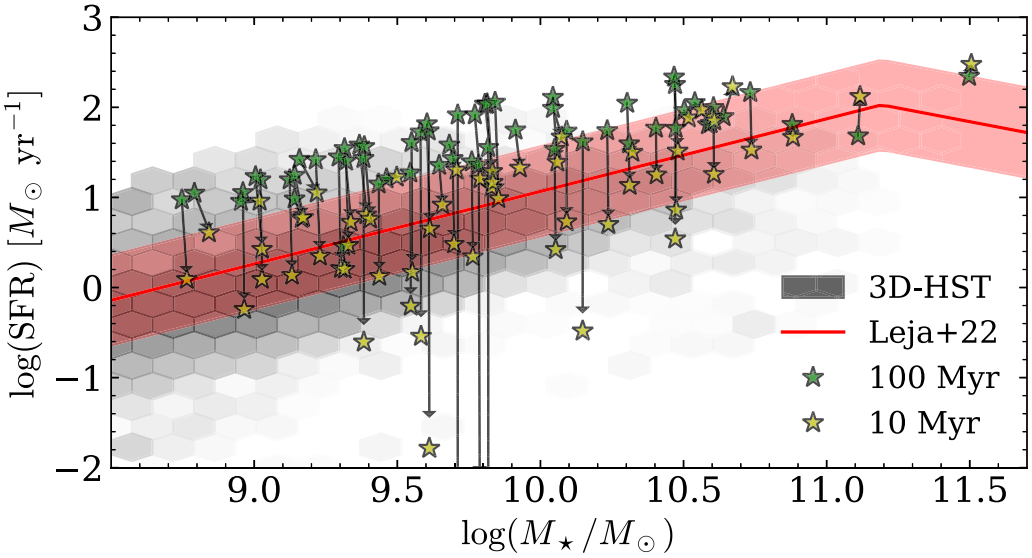

Figure 12. The majority of galaxies in our sample remain on the MS even after the central burst in SFR. Galaxies are plotted on the SFMS with their mass and SFR during two time bins, 100 and 10 Myr prior to observation, with yellow and green stars, respectively. Arrows show the SFR–stellar mass evolution in each galaxy between these two bins. The grayscale hexbins show an underlying distribution of star-forming galaxies from 3D-HST (Brammer et al. 2012). The red line shows the empirical SFMS relation from Leja et al. (2022), with the shaded region indicating a 0.5 dex scatter.

lower end of the SFMS as gas consumption and feedback stall future star formation. They suggest this behavior occurs on timescales of roughly ∼100 Myr, which is supported by the location of our galaxies on the SFMS in the 10 Myr bin, roughly 100 Myr after the increase in SFRs.

The predominance of main-sequence galaxies, combined with the notable burst in star formation just before observation, suggests that the appearance of the burst in most of these galaxies is a selection effect of studying star-forming galaxies. The fact that the galaxies in our sample are solidly within the MS, even after most of them have experienced a burst that brought them above the MS, may explain why we find no evidence of structural transformations, i.e., the shrinking of size and increase of central stellar density, that appear to accompany galaxies as they descend below the MS (Cheung et al. 2012; Barro et al. 2017; Whitaker et al. 2017; Lee et al. 2018; Ji & Giavalisco 2022): our galaxies are not yet quenching.

4.5. Star Formation Rate Gradients

Using the two-bin, spatially resolved SFHs of our galaxies, we can also attempt to measure the time evolution of the SFR gradients. SFR density gradients are computed by dividing the SFR of each component by the area of that component. For this purpose, we define the inner and outer components as concentric circular regions with central radius R (i.e., the radius used for the photometric decomposition) and Kron radius (Kron 1980), respectively. Figure 13 shows the SFR density gradients (colored lines) for all galaxies in the sample across all seven time bins. The sample median gradients are also shown as black dashed lines. As Figure 13 suggests, for much of a star-forming galaxy's history, the gradients are relatively flat, i.e., star formation builds up the inner and outer parts at approximately equal rates. This agrees with previous studies that find significant mass evolution at all radii in Milky Way progenitors (e.g., van Dokkum et al. 2013). However, significant negative gradients in star formation rate density are present across the main sequence at $z \sim 1$ (Nelson et al. 2016), a significant difference from the roughly equal growth at all radii that we seem to be observing at higher redshifts.

In our sample of main-sequence galaxies, we find a dramatic shift to negative SFR gradients ∼100 Myr prior to observation (second panel, Figure 13(a)), which we associate with a rapid build-up of the central regions in the galaxies. This is also reflected in Figure 13(b), where on average the gradients become significantly negative at a lookback time of ∼100 Myr. These negative gradients, with approximately the same slope as the gradients reported in Nelson et al. (2016), persist even after the largest increase in SFR at 100–300 Myr lookback time observed in several of our sample galaxies. Figure 14 examines the evolution of the gradients versus that of lookback time, integrated stellar mass, SFR, and sSFR. The negative gradients are the steepest when the galaxies experience the largest SFR, which, as we have seen from the SFH, happens at relatively recent lookback times from the observations, i.e., 100–300 Myr. By this time, the galaxies have also assembled nearly all of the stellar mass found at the time of observation. As the bottom panel of Figure 14 shows, however, this is not the time when the galaxies have the largest sSFR, but rather an intermediate value (in log space).

The change in SFR gradient also supports observed gas-phase metallicity gradients in star-forming galaxies. Simons et al. (2021) find that the vast majority of star-forming galaxies at $0.6 < z < 2.6$ have flat or slightly positive metallicity gradients. In order to achieve these flat gradients, most of the mass in the galaxy must be built up evenly across the galaxy, because metals are produced in stars and through stellar evolution. We measure flat SFR gradients on average across ∼96% of the galaxies' lifetimes, which supports the formation of a flat metallicity gradient. Moreover, Simons et al. (2021) find galaxies at $z \sim 0$ have negative metallicity gradients for most masses, which suggests these galaxies must also have negative metallicity gradients for much of their lifetimes. In this case, these galaxies may have shifted to a negative gradient and started to build up their centers, which produced increased gas-phase metallicities in the center.

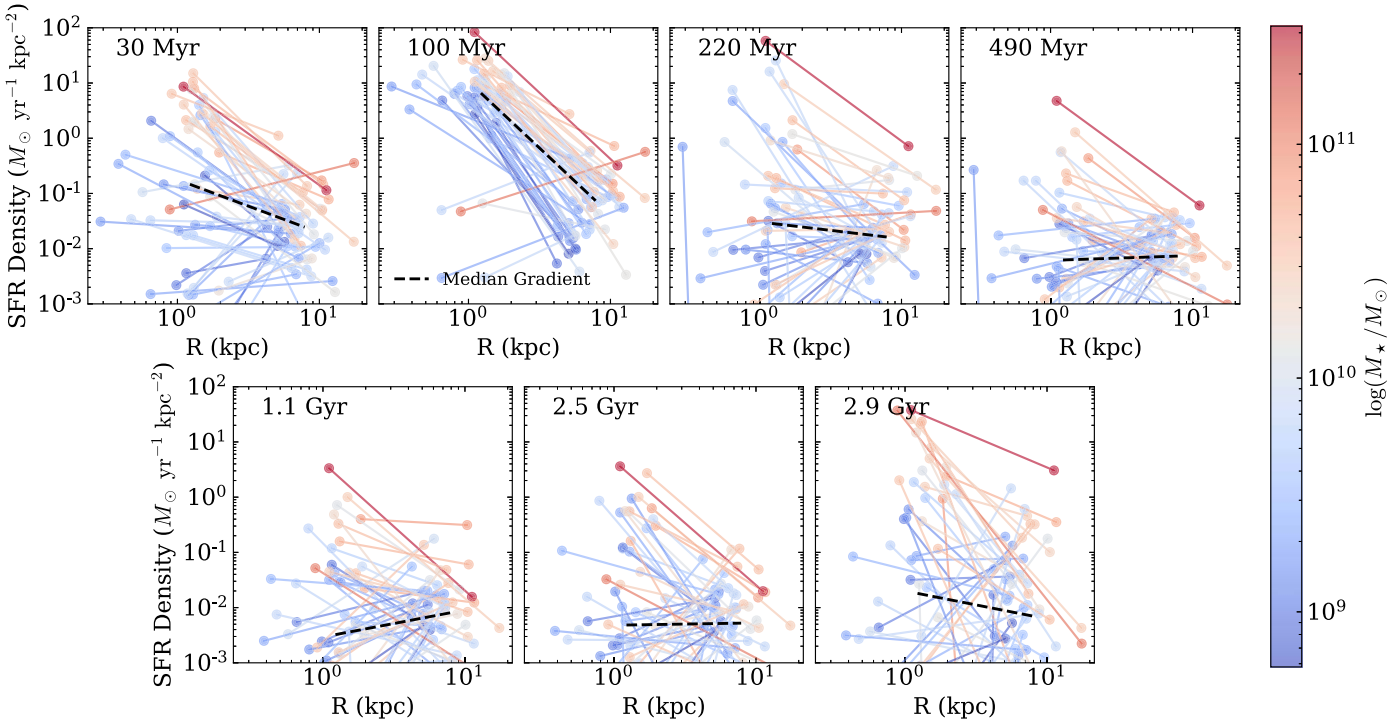

Figure 13. On average, the star formation rate gradient is flat for much of the history of galaxies in this sample. The seven panels show the individual SFR density (SFR/Area) gradients over the formation history of each galaxy in the sample with colored lines. The inner radius is defined as half the center radius R, and the outer radius is the average between R and the Kron radius measured in the CANDELS/SHARDS photometric catalogs. The seven panels indicate the upper edge of the corresponding age bin from the measured star formation histories. The color of the gradients indicates the total stellar mass of the galaxy, and the dashed black line shows the median SFR gradient.

5. Summary

In this paper, we examine the formation of dense central regions in star-forming galaxies at $z \sim 2.3$, an epoch that coincides with the formation of the bulge and chemical thick disk in the MW (Miglio et al. 2021; Queiroz et al. 2021). A sample of 60 galaxies is selected from MOSDEF (Kriek et al. 2015; Sanders et al. 2018) and the GOODS-N CANDELS/SHARDS photometric catalogs (Barro et al. 2019) with accurate photometry, spectroscopic redshifts, and metallicities. Galaxies are decomposed into central and outer components via a color-selected circular aperture, from which resolved HST photometry is measured. Using the PROSPECTOR code (Johnson et al. 2021), we fit SEDs to each galaxy in the sample using an iterative method to account for unresolved light in the ground-based K-band and Spitzer/IRAC bands.

The formation histories of these components provide an interesting insight into the differential formation of "normal" galaxies near the peak of cosmic star formation. These galaxies show strongly peaked SFHs for all but the most massive galaxies. While this means we may be observing the inside-out growth of galaxies above $\log(M_\star/M_\odot) > 10.5$, it also suggests that a rapid increase in the SFR is responsible for the formation of the centers of lower-mass galaxies. Analysis of the timescales and skewness (Equations (7) and (8), respectively) of galaxies indicates that outskirts tend to have more uniform SFHs and much longer total timescales. Conversely, galactic centers have much more uneven SFHs with short timescales, indicative of a formation history dominated by a late burst of star formation.

This increase in SFR may be due to a a gas compaction event (Dekel & Burkert 2014; Zolotov et al. 2015; Tacchella et al. 2016, 2018) or an increase in the rate at which star-forming clumps are accreted into the galactic center (Dekel et al. 2009a; van Dokkum et al. 2013), both of which should be reflected in the smaller sizes and larger central densities of galaxies with high sSFRs 100 Myr prior to observation. However, we find no trends in the age or sSFR of the central parts of galaxies with size and central density. Compaction of gas or increased clump accretion may still be possible mechanisms, but the subsequent change in morphology would not result in a more compact system.

Analysis of the SFR gradients also reveals flat gradients on average for the majority of the galactic lifetimes, in support of previous studies of the mass evolution of Milky Way progenitors (van Dokkum et al. 2013). These galaxies then transition to a steep negative gradient at ~100 Myr before observation, mirroring the inside-out growth found in studies of resolved Hα emission (Nelson et al. 2016). This evolution in the SFR gradient may also provide an explanation for the mostly flat observed metallicity gradients in main-sequence galaxies (Simons et al. 2021), which may be due to the long period of time over which these galaxies have flat SFR gradients.

We are grateful to Avishai Dekel and Cristina Chiappini for reading the manuscript and for very useful comments. We acknowledge use of observations with the NASA/ESA Hubble Space Telescope obtained from the MAST Data Archive at the Space Telescope Science Institute, which is operated by the Association of Universities for Research in Astronomy, Incorporated under NASA contract NAS5-26555. Support for Program number HST-AR-15798 was provided through a grant from the STScI under NASA contract NAS5-26555. This material is based upon work supported by the National Science

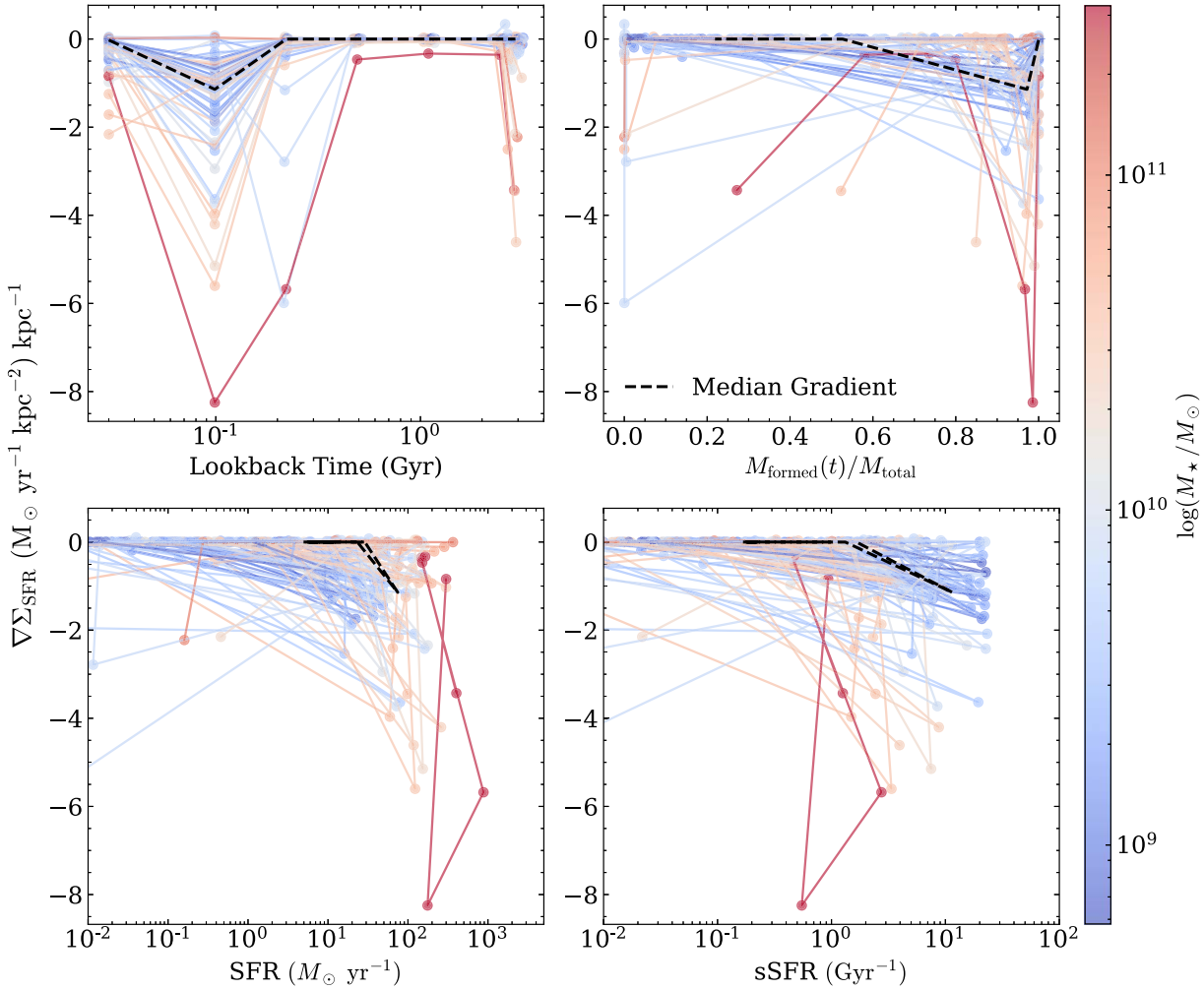

Figure 14. The evolution of the SFR density gradient ($\nabla\Sigma_{\rm SFR} \equiv \Delta\Sigma_{\rm SFR}/\Delta R$) with lookback time (top left), cumulative mass formed (top right), SFR (bottom left), and sSFR (bottom right). The symbols and coloring are the same as in Figure 13.

Foundation under Grant No. 2005578. This research made use of Montage. It is funded by the National Science Foundation under grant No. ACI-1440620 and was previously funded by the National Aeronautics and Space Administrations Earth Science Technology Office, Computation Technologies Project, under Cooperative Agreement No. NCC5-626 between NASA and the California Institute of Technology.

Facilities: HST (ACS and WFC3), KPNO (Mosaic), Subaru (MOIRCS), Spitzer (IRAC), GTC (OSIRIS).

Software: ASTROPY (Astropy Collaboration et al. 2013, 2018, 2022), PROSPECTOR (Johnson et al. 2021), FSPS (Conroy et al. 2009, 2010; Conroy & Gunn 2010), PYTHON-FSPS (Foreman-Mackey et al. 2014), EMCEE (Foreman-Mackey et al. 2013), MONTAGE (montage.ipac.caltech.edu), GALFIT (Peng et al. 2002, 2010) PHOTUTILS (Bradley et al. 2022), MATPLOTLIB (Hunter 2007), NUMPY (van der Walt et al.2011).

Appendix A
Sample Galaxy Images and Center Apertures

Figure A1 shows three-color images of the 60 galaxies in our sample and the center apertures determined in Section 3.1. The color-selected centers agree with the apparent structural centers of these galaxies.

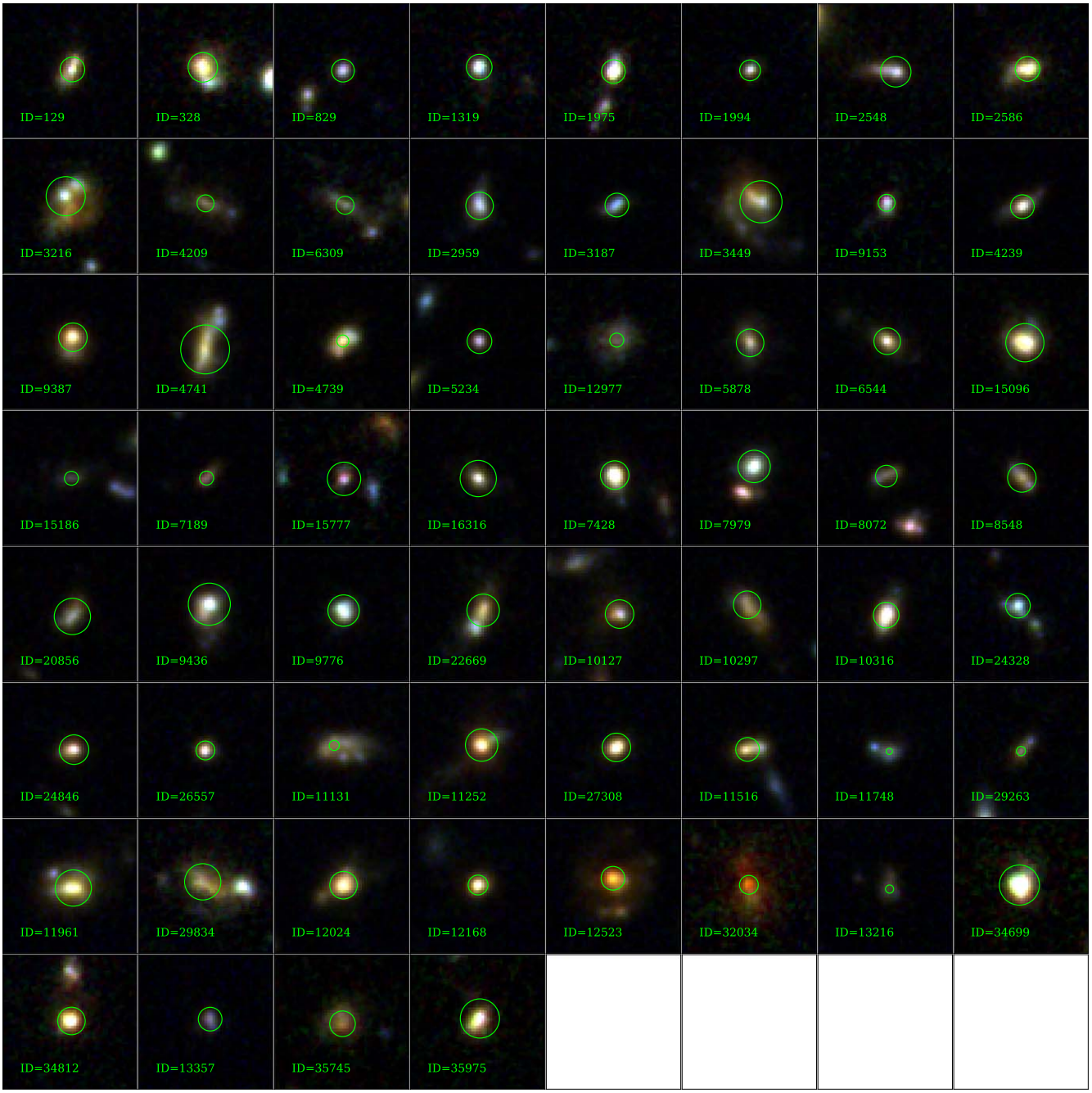

Figure A1. Three-color images (red = F160W, green = F125W, and blue = F850LP) of all 60 main-sequence galaxies in our sample. The center apertures determined by the procedure in Section 3.1 are shown in green. The IDs are from the MOSDEF survey (Kriek et al. 2015).

Appendix B
Example Posterior Distributions and Covariances

Figures B1–B3 show posterior distributions for the inner, outer, and integrated galaxy components for the example galaxy SED in Figure 3. In general, all stellar population parameters are well-constrained for both components and the total galaxy.

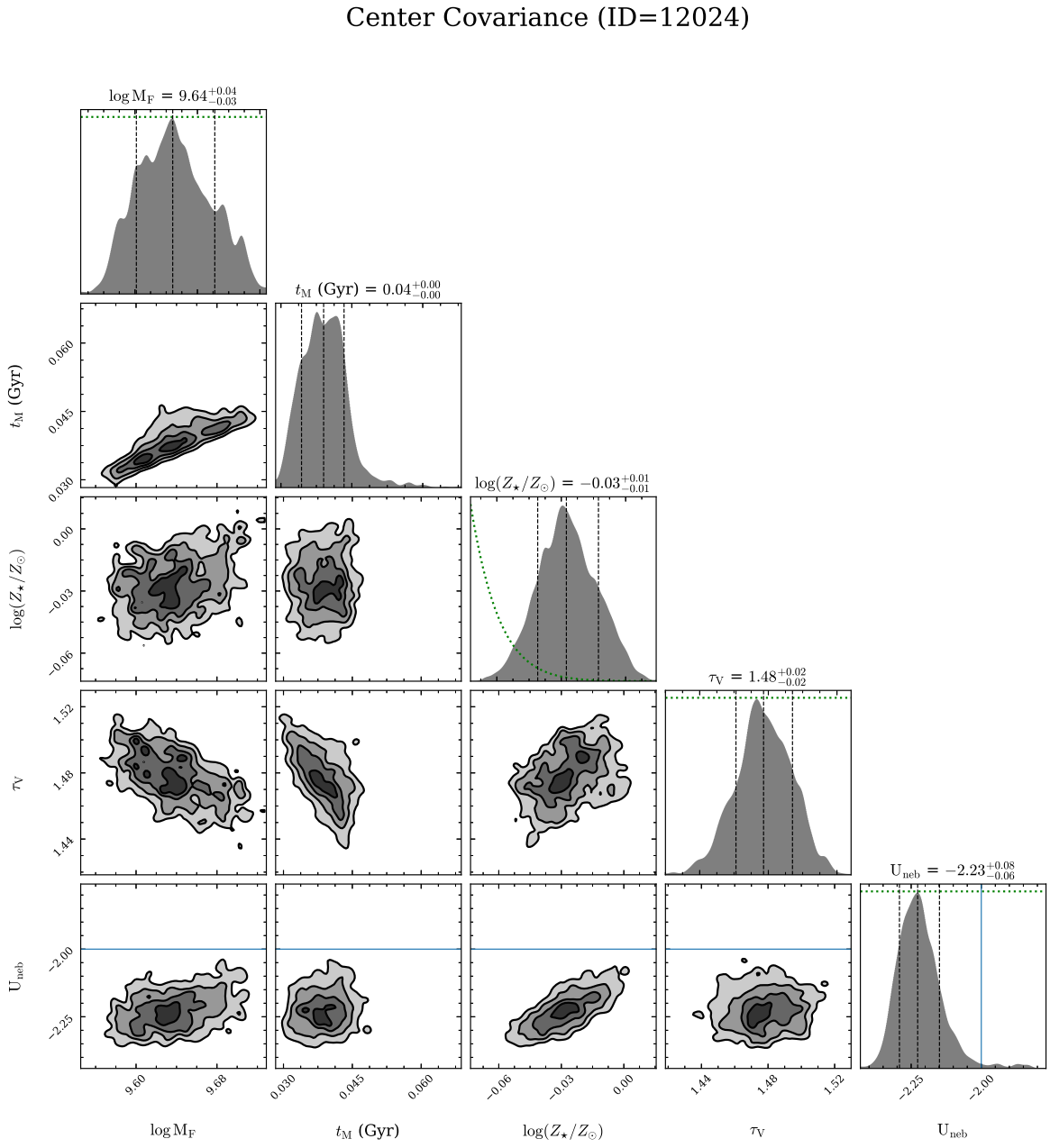

Figure B1. Corner plots showing posterior distributions of PROSPECTOR stellar population parameters for the central part of the galaxy. The included parameters are (by column, from left to right) the stellar mass ($M_\star$, not the mass formed), the mass-weighted age (t_M, transformed from the SFH), the metallicity ($\log Z$), the V-band optical depth (τ_V), and the ionization parameter ($U_{\rm neb}$). Histograms and contours show the projected 1D and 2D posterior PDFs for the listed parameters. The median value of each parameter and its uncertainties (from the 16th and 84th percentiles) are given at the top of each column. Blue lines and points indicate the initial guess given to PROSPECTOR (e.g., MOSDEF metallicities, GOODS-N masses, etc.). Priors are shown with dotted green lines. It should be noted that the stellar mass and mass-weighted age do not have initial guesses or priors, because these are transformed parameters.

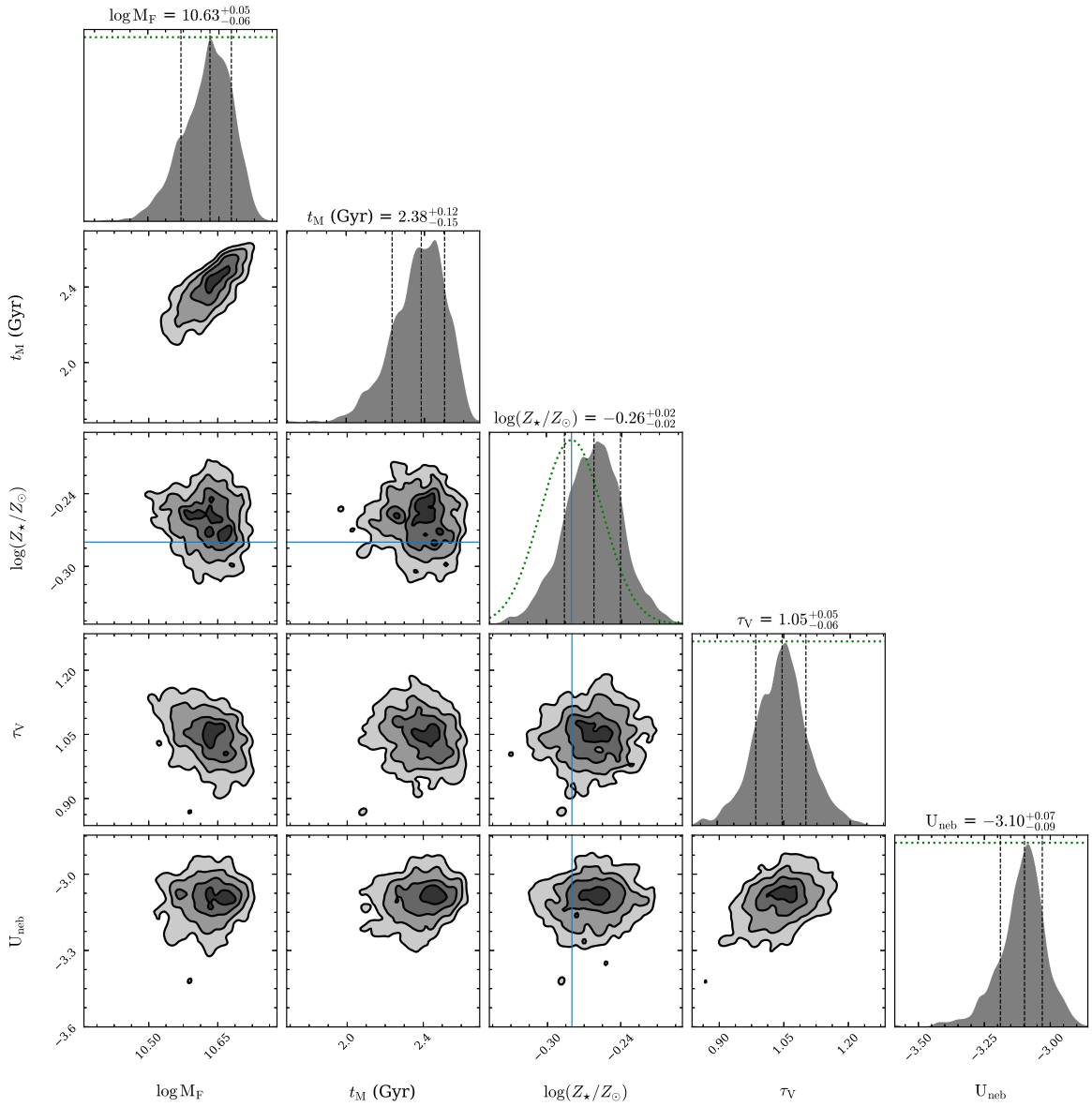

Figure B2. Same as Figure B1, but showing the outer component.

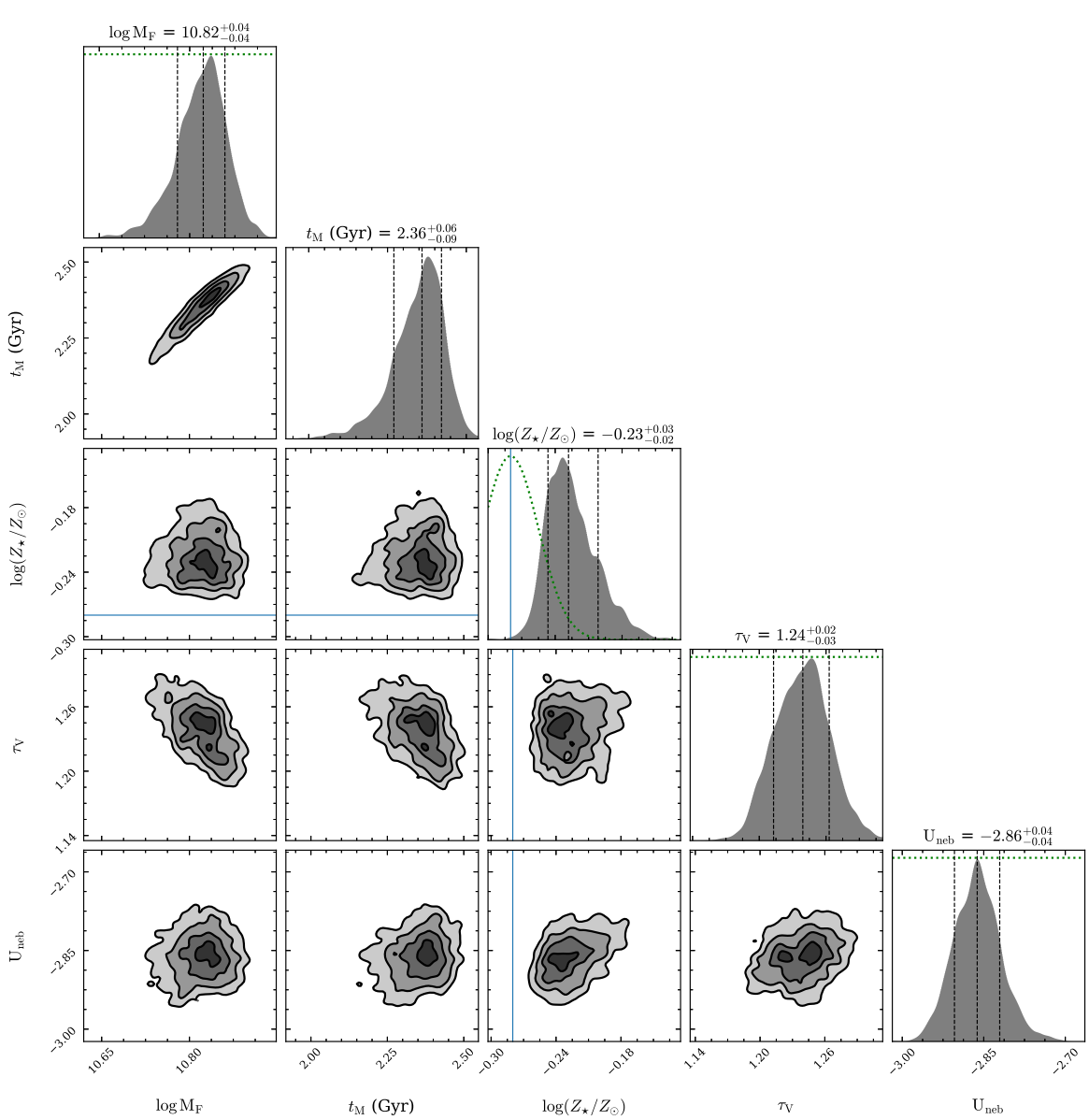

Figure B3. Same as Figure B1, but showing the population parameters for the integrated galaxy.

Appendix C
Verifying the Robustness of PROSPECTOR Star Formation Histories

We have tested the stability and robustness of our reconstruction of the integrated SFHs (i.e., the SFH of each galaxy as a whole and not of centers and outskirts) for our samples against the input photometry, the adoption of the metallicity prior, and the sampling of the lookback time: the six bins adopted in the primary runs versus the nine bins adopted here. Specifically, for each galaxy in the sample we have rerun PROSPECTOR (test runs) utilizing the expanded CANDELS photometric catalogs in the GOODS-N field, which, in addition to the HST data in the GOODS (Giavalisco et al. 2004) and CANDELS (Grogin et al. 2011; Koekemoer et al. 2011) surveys, along with the ground- and space-based ancillary data from UV to FIR, includes the 25 medium-band photometry measurements at optical wavelengths acquired during the SHARDS survey (Pérez-González et al. 2013) with the OSIRIS instrument at the 10.4 m telescope Gran Telescopio Canarias (GTC). The photometric apertures of the SHARDS data have been matched to those of the existing CANDELS data (Barro et al. 2019). The total number of photometric bands used in the PROSPECTOR SED modeling for the test runs is 42. We have then compared the SFHs obtained during these tests run with the corresponding integrated SFHs obtained with the same settings used for the SFHs of the centers and outskirts (primary runs).

We have done two test runs, namely with and without a prior on gas-phase metallicity, using the MOSDEF measures that we used for the primary runs. Also, for all test runs we have sampled the SFH in nine bins of lookback time to test the stability of the SFH with respect to the choice of the time bins. To compare the nine-bin SFH of the test runs with the six-bin

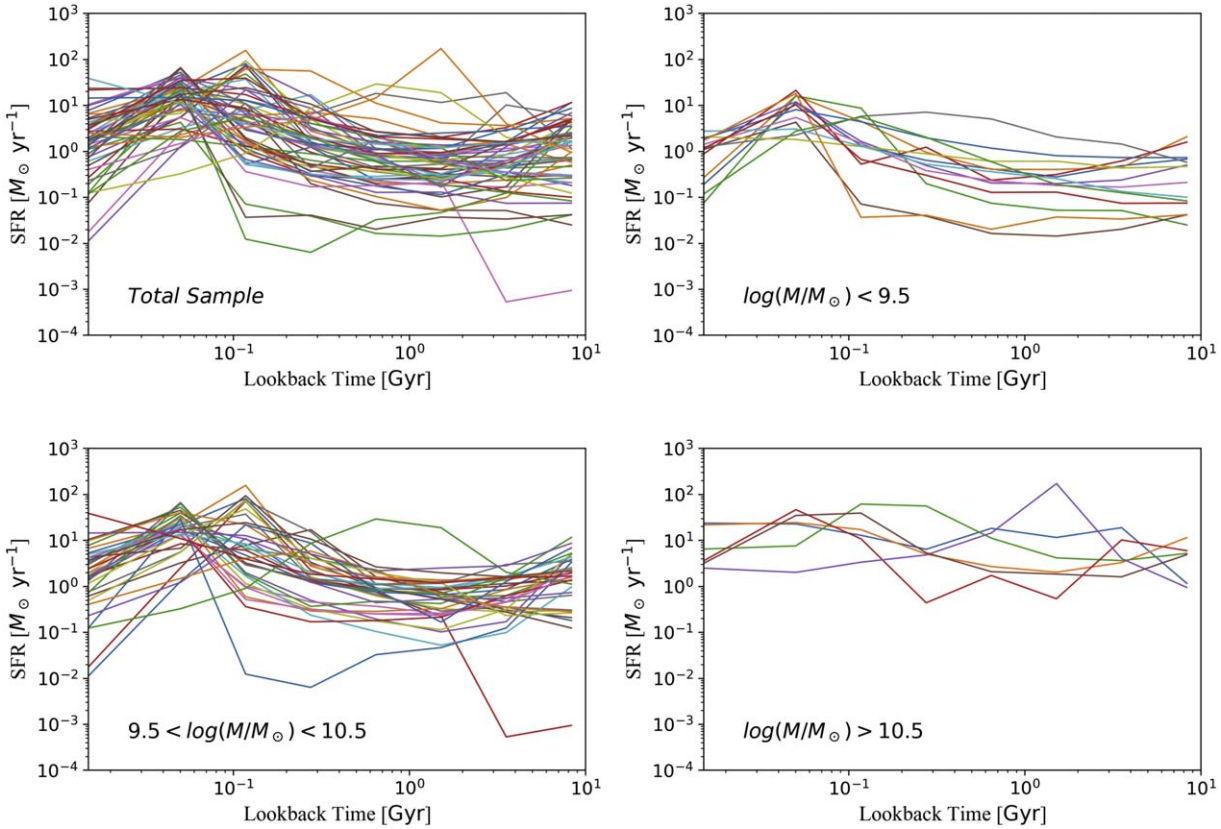

Figure C1. The individual SFHs of sample galaxies obtained during the test run for the total sample of star-forming galaxies (top left), as well as various mass bins. These test runs are fit with an increased number of photometric data points, more time bins, and no metallicity prior, to help validate the robustness of our semi-resolved SFHs. Due the very large number of photometric bands at low angular resolution, we did not attempt to decompose the photometry into "centers" and "outskirts," and only the integrated SFH has been derived. Overall, there is excellent qualitative agreement of the shape of the SFH from the two sets of runs.

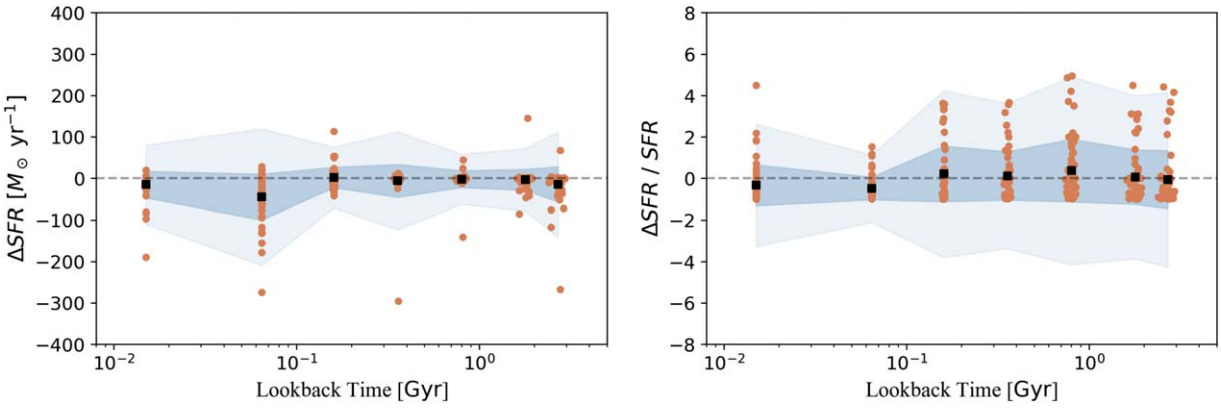

Figure C2. Overall, no systematic deviations are observed between the SFHs in our analysis (primary runs) and the SFHs from test runs with more photometry and higher time resolution (with no metallicity prior), suggesting that, on average, the shape of the reconstructed SFH is robust. The left panel shows the absolute difference between the SFH derived during the primary runs and the test runs, while the right panel shows the fractional difference. The value of the SFR of the test runs at the time bin of the primary runs has been interpolated from adjacent bins. The orange points represent the individual galaxies, the black points indicate the median, and the shaded areas show the 68th and 95th percentiles.

one for the primary runs, we perform a linear interpolation of the test-run SFHs at the central value of each primary-run time bin.

Figure C1 shows the SFHs derived during the test runs for the whole sample and in the three mass bins adopted for the primary runs. A visual comparison with the integrated SFHs derived from the primary runs shows that the shapes of the SFHs from the two sets of runs are in good qualitative agreement, suggesting that the primary-run SFHs are robust. Figure C2 quantifies the difference between the output of the sets of run: the left panel shows the absolute difference of the SFH of each galaxy in the two sets of runs, while the left panel shows the fractional difference. It can be seen that the median difference between the two sets of runs is essentially zero for all values of the lookback time, while the scatter remains small for the three most recent time bins and it only increases at large

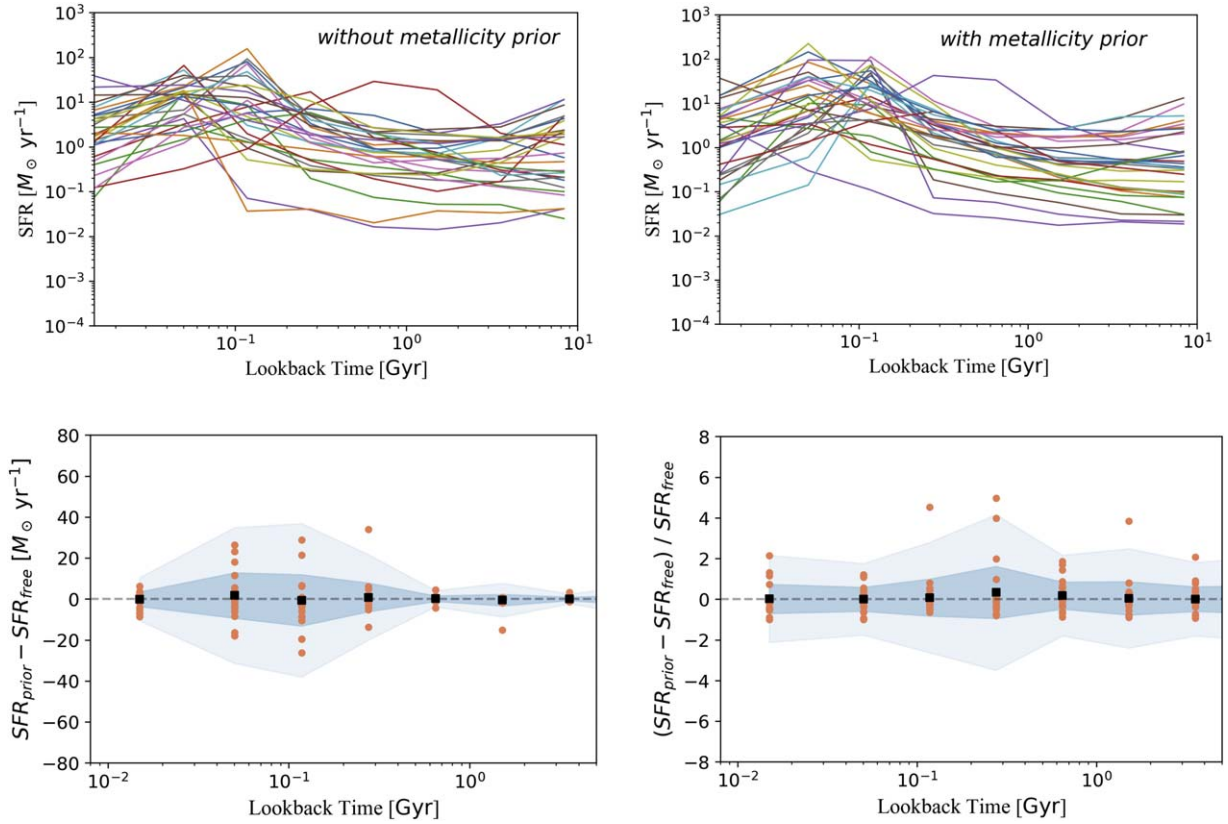

Figure C3. No systematic difference is observed between runs with and without a prior on the metallicity. The top panels show individual SFHs obtained during the test runs, with (right) and without (left) adopting a metallicity prior. Overall, the shape of the SFH is qualitatively fairly insensitive to the prior, and only small differences are observed. The bottom panels show the absolute (left) and fractional (right) differences in the SFHs, respectively, with and without the prior. The shaded areas indicate the 68th (blue) and 95th (light blue) percentile ranges.

values of the lookback time, highlighting the difficulty of reconstructing the earliest phases of the SFH. Fortunately, the key results of this work are based on the difference of the SFHs of "centers" and "outskirts" during later stages of their evolution, at lookback times close to the time of observation. Overall, the agreement between the primary and test runs appears to be very good, demonstrating that the overall shape of the SFH is insensitive to the details of the input SED.

Finally, Figure C3 illustrates the sensitivity of the output SFH to the gas-phase metallicity prior. This test is relevant for this work because, during the primary runs, the same metallicity prior is used for both the centers and the outskirts. A strong dependence of the SFH on the metallicity prior would have diminished the significance of the difference that we have observed for the two regions of the galaxies. As the figures illustrate, the test reveals only small differences in the output SFH, suggesting a small sensitivity to the metallicity prior. These differences are substantially smaller than the differences of the SFHs of centers and outskirts, suggesting that they are very unlikely the result of of the oversimplification of assigning the same metallicity to both regions of the galaxies. The bottom panels of Figure C3 show the difference between the SFH derived adopting a strong prior on the gas-phase metallicity versus that derived without such a prior. No systematic difference is observed, on average, between the two cases, with the scatter of the fractional difference (bottom left panel) remaining approximately constant with lookback time.

Overall, the test runs show that the overall reconstruction of the SFHs of the sample galaxies is robust against the input photometry and the assumption of the metallicity prior, supporting the validity of our conclusions.

ORCID iDs

Sam E. Cutler https://orcid.org/0000-0002-7031-2865
Mauro Giavalisco https://orcid.org/0000-0002-7831-8751
Zhiyuan Ji https://orcid.org/0000-0001-7673-2257
Yingjie Cheng https://orcid.org/0000-0001-8551-071X

References

Abramson, L. E., Kelson, D. D., Dressler, A., et al. 2014, ApJL, 785, L36
Ashby, M. L. N., Willner, S. P., Fazio, G. G., et al. 2013, ApJ, 769, 80
Asplund, M., Grevesse, N., Sauval, A. J., & Scott, P. 2009, ARA&A, 47, 481
Astropy Collaboration, Price-Whelan, A. M., Lim, P. L., et al. 2022, ApJ, 935, 167
Astropy Collaboration, Price-Whelan, A. M., Sipőcz, B. M., et al. 2018, AJ, 156, 123
Astropy Collaboration, Robitaille, T. P., Tollerud, E. J., et al. 2013, A&A, 558, A33
Barbuy, B., Chiappini, C., & Gerhard, O. 2018, ARA&A, 56, 223
Barro, G., Faber, S. M., Koo, D. C., et al. 2017, ApJ, 840, 47
Barro, G., Pérez-González, P. G., Cava, A., et al. 2019, ApJS, 243, 22
Bensby, T., Feltzing, S., Gould, A., et al. 2017, A&A, 605, A89
Bradley, L., Sipőcz, B., Robitaille, T., et al. 2022, astropy/photutils: v1.5.0, Zenodo, doi:10.5281/zenodo.6825092
Brammer, G. B., van Dokkum, P. G., Franx, M., et al. 2012, ApJS, 200, 13
Capak, P., Cowie, L. L., Hu, E. M., et al. 2004, AJ, 127, 180
Carrasco, E. R., Conselice, C. J., & Trujillo, I. 2010, MNRAS, 405, 2253
Ceverino, D., Dekel, A., Tweed, D., & Primack, J. 2015, MNRAS, 447, 3291
Chen, Z., Faber, S. M., Koo, D. C., et al. 2020, ApJ, 897, 102
Cheung, E., Faber, S. M., Koo, D. C., et al. 2012, ApJ, 760, 131
Coil, A. L., Aird, J., Reddy, N., et al. 2015, ApJ, 801, 35

Conroy, C. 2013, ARA&A, 51, 393
Conroy, C., & Gunn, J. E. 2010, ApJ, 712, 833
Conroy, C., Gunn, J. E., & White, M. 2009, ApJ, 699, 486
Conroy, C., White, M., & Gunn, J. E. 2010, ApJ, 708, 58
Cutler, S. E., Whitaker, K. E., Mowla, L. A., et al. 2022, ApJ, 925, 34
Dekel, A., Birnboim, Y., Engel, G., et al. 2009a, Natur, 457, 451
Dekel, A., & Burkert, A. 2014, MNRAS, 438, 1870
Dekel, A., Lapiner, S., & Dubois, Y. 2019, arXiv:1904.08431
Dekel, A., Sari, R., & Ceverino, D. 2009b, ApJ, 703, 785
Dickinson, M., Bergeron, J., Casertano, S., et al. 2003, Great Observatories Origins Deep Survey (GOODS) Validation Observations, Spitzer Proposal ID 196
Dimauro, P., Daddi, E., Shankar, F., et al. 2022, MNRAS, 513, 256
Elbaz, D., Leiton, R., Nagar, N., et al. 2018, A&A, 616, A110
Elmegreen, B. G., Bournaud, F., & Elmegreen, D. M. 2008, ApJ, 688, 67
Fagioli, M., Carollo, C. M., Renzini, A., et al. 2016, ApJ, 831, 173
Fetherolf, T., Reddy, N. A., Shapley, A. E., et al. 2020, MNRAS, 498, 5009
Foreman-Mackey, D., Hogg, D. W., Lang, D., & Goodman, J. 2013, PASP, 125, 306
Foreman-Mackey, D., Sick, J., & Johnson, B. 2014, python-fsps: Python bindings to FSPS (v0.1.1), v0.1.1, Zenodo, doi:10.5281/zenodo.12157
Franco, M., Elbaz, D., Zhou, L., et al. 2020, A&A, 643, A30
Genzel, R., Förster Schreiber, N. M., Übler, H., et al. 2017, Natur, 543, 397
Genzel, R., Price, S. H., Übler, H., et al. 2020, ApJ, 902, 98
Giavalisco, M. 2002, ARA&A, 40, 579
Giavalisco, M., Ferguson, H. C., Koekemoer, A. M., et al. 2004, ApJL, 600, L93
Giavalisco, M., Steidel, C. C., & Macchetto, F. D. 1996, ApJ, 470, 189
Gómez-Guijarro, C., Elbaz, D., Xiao, M., et al. 2022, A&A, 659, A196
Grogin, N. A., Kocevski, D. D., Faber, S. M., et al. 2011, ApJS, 197, 35
Guo, K., Zheng, X. Z., Wang, T., & Fu, H. 2015, ApJL, 808, L49
Guo, Y., Giavalisco, M., Ferguson, H. C., Cassata, P., & Koekemoer, A. M. 2012, ApJ, 757, 120
Häring, N., & Rix, H.-W. 2004, ApJL, 604, L89
Huertas-Company, M., Guo, Y., Ginzburg, O., et al. 2020, MNRAS, 499, 814
Hunter, J. D. 2007, CSE, 9, 90
Inoue, T., & Inutsuka, S.-i. 2016, ApJ, 833, 10
Ji, Z., & Giavalisco, M. 2022, ApJ, 935, 120
Johnson, B. D., Leja, J., Conroy, C., & Speagle, J. S. 2021, ApJS, 254, 22
Kajisawa, M., Ichikawa, T., Tanaka, I., et al. 2011, PASJ, 63, 379
Kauffmann, G., Heckman, T. M., Simon White, D. M., et al. 2003, MNRAS, 341, 33
Kereš, D., Katz, N., Weinberg, D. H., & Davé, R. 2005, MNRAS, 363, 2
Koekemoer, A. M., Faber, S. M., Ferguson, H. C., et al. 2011, ApJS, 197, 36
Kormendy, J., & Ho, L. C. 2013, ARA&A, 51, 511
Kormendy, J., & Kennicutt, R. C., Jr. 2004, ARA&A, 42, 603
Kriek, M., Shapley, A. E., Reddy, N. A., et al. 2015, ApJS, 218, 15
Kriek, M., van Dokkum, P. G., Labbé, I., et al. 2009, ApJ, 700, 221
Kron, R. G. 1980, ApJS, 43, 305
Kroupa, P. 2001, MNRAS, 322, 231
Lee, B., Giavalisco, M., Whitaker, K., et al. 2018, ApJ, 853, 131
Leja, J., Carnall, A. C., Johnson, B. D., Conroy, C., & Speagle, J. S. 2019, ApJ, 876, 3
Leja, J., Speagle, J. S., Ting, Y.-S., et al. 2022, ApJ, 936, 165
Leja, J., van Dokkum, P. G., Momcheva, I., et al. 2013, ApJL, 778, L24
Liu, D., Daddi, E., Dickinson, M., et al. 2018, ApJ, 853, 172
Mandelker, N., Dekel, A., Ceverino, D., et al. 2017, MNRAS, 464, 635
Marinacci, F., Vogelsberger, M., Pakmor, R., et al. 2018, MNRAS, 480, 5113
Martig, M., Bournaud, F., Teyssier, R., & Dekel, A. 2009, ApJ, 707, 250
Miglio, A., Chiappini, C., Mackereth, J. T., et al. 2021, A&A, 645, A85
Mobasher, B., Dahlen, T., Ferguson, H. C., et al. 2015, ApJ, 808, 101
Mosleh, M., Hosseinnejad, S., Hosseini-ShahiSavandi, S. Z., & Tacchella, S. 2020, ApJ, 905, 170
Naiman, J. P., Pillepich, A., Springel, V., et al. 2018, MNRAS, 477, 1206
Nelson, D., Pillepich, A., Springel, V., et al. 2018, MNRAS, 475, 624
Nelson, D., Pillepich, A., Springel, V., et al. 2019a, MNRAS, 490, 3234
Nelson, E. J., Tadaki, K.-i., Tacconi, L. J., et al. 2019b, ApJ, 870, 130
Nelson, E. J., van Dokkum, P. G., Förster Schreiber, N. M., et al. 2016, ApJ, 828, 27
Newman, A. B., Belli, S., Ellis, R. S., & Patel, S. G. 2018, ApJ, 862, 126
Ocvirk, P., Pichon, C., Lançon, A., & Thiébaut, E. 2006, MNRAS, 365, 46
Papovich, C., Dickinson, M., & Ferguson, H. C. 2001, ApJ, 559, 620
Papovich, C., Dickinson, M., Ferguson, H. C., et al. 2004, ApJL, 600, L111
Peng, C. Y., Ho, L. C., Impey, C. D., & Rix, H.-W. 2002, AJ, 124, 266
Peng, C. Y., Ho, L. C., Impey, C. D., & Rix, H.-W. 2010, AJ, 139, 2097
Pérez-González, P. G., Cava, A., Barro, G., et al. 2013, ApJ, 762, 46
Pforr, J., Maraston, C., & Tonini, C. 2012, MNRAS, 422, 3285
Pforr, J., Maraston, C., & Tonini, C. 2013, MNRAS, 435, 1389
Pillepich, A., Nelson, D., Hernquist, L., et al. 2018, MNRAS, 475, 648
Pillepich, A., Nelson, D., Springel, V., et al. 2019, MNRAS, 490, 3196
Puglisi, A., Daddi, E., Liu, D., et al. 2019, ApJL, 877, L23
Puglisi, A., Daddi, E., Valentino, F., et al. 2021, MNRAS, 508, 5217
Queiroz, A. B. A., Anders, F., Chiappini, C., et al. 2020, A&A, 638, A76
Queiroz, A. B. A., Chiappini, C., Perez-Villegas, A., et al. 2021, A&A, 656, A156
Renzini, A. 2020, MNRAS, 495, L42
Sanders, R. L., Shapley, A. E., Kriek, M., et al. 2018, ApJ, 858, 99
Schreiber, C., Elbaz, D., Pannella, M., et al. 2016, A&A, 589, A35
Shapley, A. E., Steidel, C. C., Adelberger, K. L., et al. 2001, ApJ, 562, 95
Shen, S., Mo, H. J., White, S. D. M., et al. 2003, MNRAS, 343, 978
Simons, R. C., Papovich, C., Momcheva, I., et al. 2021, ApJ, 923, 203
Springel, V., Pakmor, R., Pillepich, A., et al. 2018, MNRAS, 475, 676
Steidel, C. C., Erb, D. K., Shapley, A. E., et al. 2010, ApJ, 717, 289
Steidel, C. C., Giavalisco, M., Dickinson, M., & Adelberger, K. L. 1996, AJ, 112, 352
Tacchella, S., Carollo, C. M., Faber, S. M., et al. 2017, ApJL, 844, L1
Tacchella, S., Carollo, C. M., Förster, N. M., et al. 2018, ApJ, 859, 56
Tacchella, S., Conroy, C., Faber, S. M., et al. 2022, ApJ, 926, 134
Tacchella, S., Dekel, A., Carollo, C. M., et al. 2016, MNRAS, 457, 2790
Tadaki, K.-i., Belli, S., Burkert, A., et al. 2020, ApJ, 901, 74
Tadaki, K.-i., Kodama, T., Nelson, E. J., et al. 2017, ApJL, 841, L25
van der Walt, S., Colbert, S. C., & Varoquaux, G. 2011, CSE, 13, 22
van der Wel, A., Chang, Y.-Y., Bell, E. F., et al. 2014a, ApJL, 792, L6
van der Wel, A., Franx, M., van Dokkum, P. G., et al. 2014b, ApJ, 788, 28
van Dokkum, P. G., Bezanson, R., van der Wel, A., et al. 2014, ApJ, 791, 45
van Dokkum, P. G., Leja, J., Nelson, E. J., et al. 2013, ApJL, 771, L35
van Dokkum, P. G., Whitaker, K. E., Brammer, G., et al. 2010, ApJ, 709, 1018
Webb, T. M., Eales, S., Foucaud, S., et al. 2003, ApJ, 582, 6
Whitaker, K. E., Bezanson, R., van Dokkum, P. G., et al. 2017, ApJ, 838, 19
Whitney, A., Conselice, C. J., Bhatawdekar, R., & Duncan, K. 2019, ApJ, 887, 113
Wild, V., Walcher, C. J., Johansson, P. H., et al. 2009, MNRAS, 395, 144
Williams, C. C., Giavalisco, M., Bezanson, R., et al. 2017, ApJ, 838, 94
Williams, C. C., Giavalisco, M., Cassata, P., et al. 2014, ApJ, 780, 1
Zolotov, A., Dekel, A., Mandelker, N., et al. 2015, MNRAS, 450, 2327